

Chapter 3: Elastic-Plastic Indentation Experiments

This chapter will begin by addressing fundamental contact mechanics issues in nanoindentation testing and analysis. The analysis will be limited to elastic-plastic (time-independent) materials and systems. Elastic-plastic indentation testing and analysis will then be applied to examine mechanical behavior of mineralized biological tissues including an examination of length-scale effects in indentation measurements. Finally, a new technique is developed for indentation mechanical property mapping in two-dimensions.

3.1 Elastic-Plastic Indentation Analysis

A number of assumptions are built into the everyday operation of mechanical testing devices, and nanoindentation devices in particular, even when the materials being tested are “simple” (e.g. homogeneous, time-independent) engineering metals and glasses. Key issues associated specifically with nanoindentation testing will be discussed here in detail within the context of time-independent materials (or materials with limited time-dependent responses); the issue of time-dependence will be addressed in Chapter 4.

A critical assumption in indentation testing is that the instrument-tip combination have been calibrated correctly to allow for the measurement of quantitative material property information from the indentation test data. Another question arises as to whether the assumptions in the Oliver-Pharr analysis, built into the instrument software and used for Berkovich elastic-plastic indentation analysis of stiff engineering materials, are valid for compliant materials. Finally, the frequently-reported relationship between elastic modulus and contact hardness will be critically examined.

3.1.1 Calibration

Nanoindentation is a “garbage in, garbage out” mechanical testing modality, particularly in the modern age of semi-automated instruments. As with any mechanical test, the raw load-displacement data is always available to the user, but material properties such as elastic modulus can only be obtained following instrument calibration and advanced data analysis. In addition to the intrinsic machine compliance present in all mechanical testing devices, in indentation testing the diamond (or tungsten, alumina, or other stiff material) tip contacting the sample must be carefully calibrated and frequently evaluated. Surprisingly little has been written and published in the indentation literature on the specific details of instrument calibration or issues such as error propagation due to poor calibration. Therefore, the procedure will be described here in brief. Data will be presented illustrating the calibrated modulus-depth data for several materials,

demonstrating that the indentation testing performed in the current investigation is indeed quantitative and obtained from an instrument that was well-calibrated.

3.1.1.1 Typical Area Function Calibration

Quantitative evaluation of the elastic modulus (E') and contact hardness (H_c) for an indentation test is completely dependent on knowledge of the indenter-sample contact area (Eqn. 2-15). For commonly-utilized elastic-plastic DSI data analysis [Oliver and Pharr, 1992], the contact area of indentation is not measured directly using any microscope visualization or related technique, but is inferred from the indentation data. The fidelity of this inference relies directly on a careful calibration and frequent verification of the calibration.

The philosophy of the calibration protocol is simple: perform indentation tests on a material with well-known mechanical properties, and deduce the contact area implicitly, finding the area function required to obtain the expected mechanical properties on the well-known material. (An additional, and extremely useful step, is to then test the area function on one or more additional materials with reasonably well-known mechanical properties).

The form of the contact area function, the function that relates depth in the material to the projected contact area, is assumed to be (Eqn. 2-8; [Oliver and Pharr, 1992]):

$$A(h_c) = C_0 h_c^2 + C_1 h_c + C_2 h_c^{1/2} + \dots \quad [3-1]$$

Practically speaking, these first three terms are dominant, and in many cases, the first two are sufficient [Thurn and Cook, 2002]. Identification of the area coefficients C_i along with identification of the frame compliance C_f together comprise the overall calibration. (Frame compliance effects in calibration will be discussed in the following section).

Indentation tests for calibration purposes are performed using constant loading

rate tests (triangular or trapezoidal loading) on a fused silica standard sample at different peak load levels, typically in a logarithmic series (e.g. 0.1, 0.3, 1, 3, 10, 30, 100, 300 mN).

As in standard Oliver-Pharr data analysis, three parameters (P_{\max} , h_{\max} , S) are obtained directly from the raw load-displacement ($P-h$) data. From these parameters, the contact depth is calculated :

$$h_c = h_{\max} - \epsilon \frac{P_{\max}}{S} \quad [3-2]$$

where $\epsilon=0.75$. The reduced elastic modulus (E_R , Eqn. 2-16) of fused silica is “forced” to a fixed value (e.g. the known fused silica value for a diamond indenter, 69.6 GPa) and the contact area for each indent is calculated:

$$A_c = \frac{S^2 \pi}{4 E_R^2} = \frac{\pi}{4 E_R^2} \frac{1}{C^2} \quad [3-3]$$

where C = compliance, the inverse of the stiffness. Based on this calculation of area from Eqn. 3-3 and the independent calculation of contact depth (Eqn. 3-2), the A_c-h_c data are fit to a polynomial of the form Eqn. 3-1. The elastic modulus is then re-calculated for all indentation tests using the area function obtained from the polynomial fit.

This technique is simple and straightforward, although in practice it is prone to errors resulting from both the curve-fitting and the enforced numerical value of the elastic modulus. Fine-tuning of the area function is usually required, in which the area coefficients C_i are adjusted, and the contact area re-calculated (along with E_R and H_c) until the elastic modulus for one or more materials is constant with depth (but not necessarily of a “forced”, known numerical value).

Verification (and in some cases, fine-tuning or adjustments) of area function calibration is easily performed using continuous stiffness measurements (section 2.1.6.1),

in which the modulus can be explicitly evaluated over a wide range of indentation depths. The small depth quantitative nature of the calibrated area function used in the current work is demonstrated in a stiff material (fused silica, Figure 3-1). The large-displacement (3-10 μm) quantitative nature of the area function is demonstrated in a substantially more compliant elastomer (polyurethane, Figure 3-2).

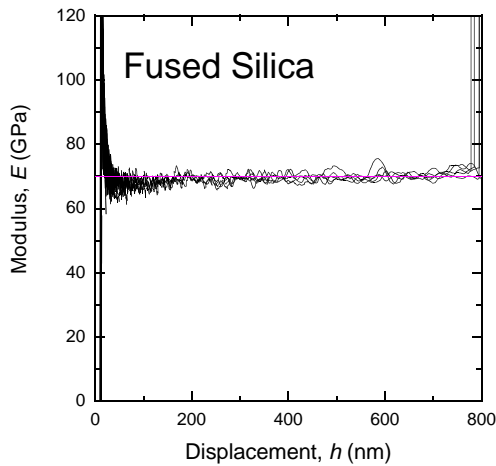


Figure 3-1: Elastic modulus (E) versus depth (h) for fused silica using continuous stiffness measurements (CSM) at very small depths.

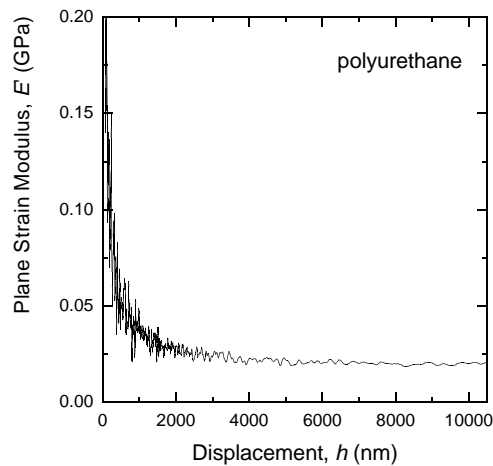


Figure 3-2: Plane strain modulus (E') versus depth (h) for polyurethane using continuous stiffness measurements (CSM) at very large depths.

The discussion of area function calibration to this point was described in isolation (*e.g.* assuming the frame compliance was correctly set); the following section will examine frame compliance effects in area function calibration.

3.1.1.2 Frame Compliance Effects in Calibration

A problem arises in this analysis in that the measured sample stiffness S may be influenced by the compliance of the materials testing machine itself. This is a well-known issue in materials testing, but takes on extra importance in nanoindentation devices compared to relatively stiff test-frames used for tensile testing at larger load- and length-scales. Thus the calculated area function may have an artifact due to this machine frame compliance, C_f , which must be calibrated separately. The level of importance of the frame compliance calibration actually varies due to both hardware and software differences, as discussed here for two of the major indentation device manufacturers, Hysitron and MTS. The Hysitron transducer is inherently more compliant than that used in the MTS testing system, (approximately one order of magnitude: compare compliance values reported in [Thurn and Cook, 2002] to the Hysitron data below) likely due to the different designs of the support springs. Therefore, accurate compliance calibration is intrinsically more important in quantitative indentation analysis using the Hysitron instrument. In addition to this magnitude difference, the MTS transducer is compliance calibrated at the time of installation and this value is inserted in a protected location in the software. (There is a user-level “frame compliance correction” that can be introduced, and this may be a positive or negative value since it is merely a small correction to a compliance value already set in the software, but this correction is seldom large and is frequently not necessary.) The frame compliance value in the Hysitron systems is a user-level software level input which could be changed from day to day, test to test, and instrument user to instrument user. Because of these differences between instrument manufacturers, the discussion of frame compliance calibration from this point forward will be conducted exclusively in the framework of the Hysitron indentation

instrument and its associated software. This discussion will also be limited to technique) for the area function calibration above (this protocol is built into the Hysitron software calibration module).

For simplicity (and partially owing to the work of Thurn and Cook [2002] who demonstrated the physical meaning of a simple quadratic function), an area function of the form:

$$A_c(h_c) = C_0 h_c^2 + C_1 h_c \quad [3-4]$$

will be used during the following analysis of calibration error. It is noted that the area function for a perfect Berkovich (3-sided) or Vickers (4-sided) pyramidal tip (with no rounding and no bluntness at the tip) gives $C_0 = 24.5$ and $C_1 = C_2 = C_3 = \dots = 0$.

In a frame compliance correction (for indenters or for servohydraulic or electromechanical test-frames) it is typically assumed that the total measured experimental stiffness is the series combination of the sample stiffness and the frame stiffness:

$$\frac{1}{S} = \frac{1}{S_{\text{sample}}} + \frac{1}{S_{\text{frame}}} \quad [3-5]$$

or, written in terms of the compliance

$$S^{-1} = C = C_{\text{sample}} + C_{\text{frame}} \quad [3-6]$$

The frame stiffness (or compliance) must be taken into account (subtracted off the measured stiffness or compliance) to accurately obtain sample elastic modulus from sample stiffness. Conversely, the frame compliance must be accounted for in the calibration of the tip area function, such that equation 3-3 becomes

$$A_c = \frac{S_{\text{sample}}^2 \pi}{4 E_R^2} = \frac{\pi}{4 E_R^2} \frac{1}{(C - C_f)^2} \quad [3-7]$$

The tip area function and frame compliance can then be calculated through an iterative procedure (albeit one which has been found to be unstable based on anecdotal evidence). It is because of the difficulty (and instability) associated with this iterative process that the following new protocol was established.

The Hysitron software is employed for the current study, in which a set of real, experimentally obtained, fused silica indentation traces are analyzed and a calibration is determined as objectively as possible. In order to obtain this calibration, a new technique is developed to try and avoid the intrinsic iterative nature of the calibration protocol proposed in the original Oliver-Pharr paper and discussed in the previous paragraph. In this investigation, the frame compliance is purposefully changed over a range of values, meant to be both larger and smaller than the expected range of machine compliance seen for the instrument. A new area function is calculated to correspond to each frame compliance value that was set. The original fused silica data is analyzed with each different calibration pair (machine compliance and area function). The overall objective of this process is two-fold: (a) to examine the effects of machine compliance on different aspects of indentation analysis, and (b) to arrive at a correct value of the machine compliance and thus a correct calibration for the instrument by eliminating the incorrect calibration pairs through objective measures.

Indentation tests were analyzed for peak load levels of 0.1, 0.5, 1, 2, 5, 8, 10, 12, and 14 mN. The frame compliance C_f was varied from 0 to 4 nm/mN and the effects of frame compliance on the calibration parameters was examined.

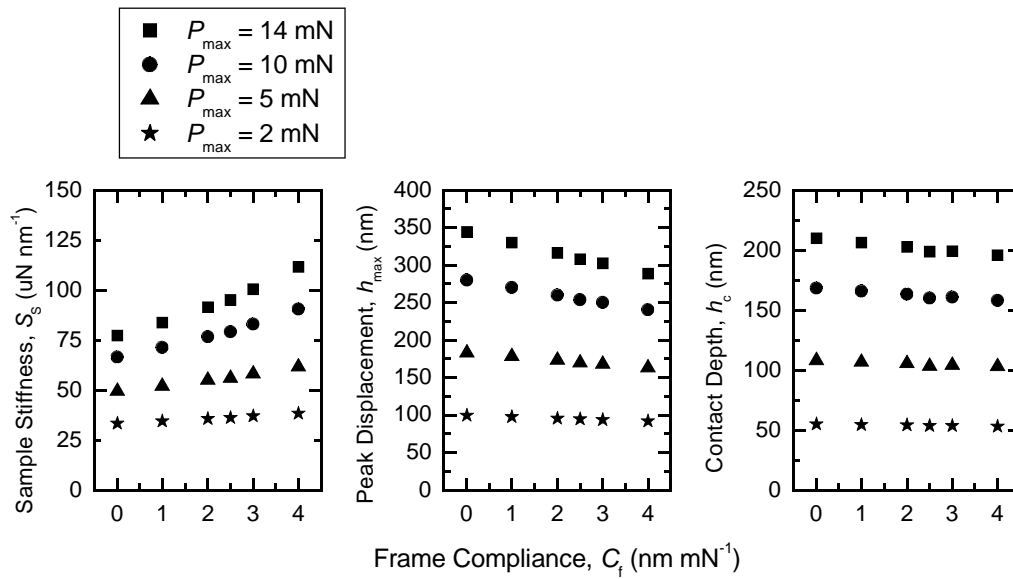


Figure 3-3: Raw peak displacement (h_{max}), sample stiffness (S) and calculated contact displacement (h_c , Eqn. 3-2) for fused silica indentation tests at four different load levels and six different frame compliance values.

The effect on the sample stiffness, S , the peak displacement, h_{max} , and the calculated contact displacement, h_c (Eqn. 3-2) from artificially altering the frame compliance, C_f , is shown in Figure 3-3 for four indentation tests at different peak load levels ($P_{max} = 2, 5, 10, 14$ mN). Interestingly, changes in S and h_{max} with C_f essentially offset, leaving little effect on the calculated contact displacement h_c .

In contrast, the contact area A_c for each indent (Eqn 3-7), is proportional to the square of the stiffness, shown experimentally in Figure 3-4. For the fused silica indentation test performed at 14 mN, the calculated area more than doubles from one million to over two million square nanometers over the range of experimentally-altered frame compliance values examined in this investigation.

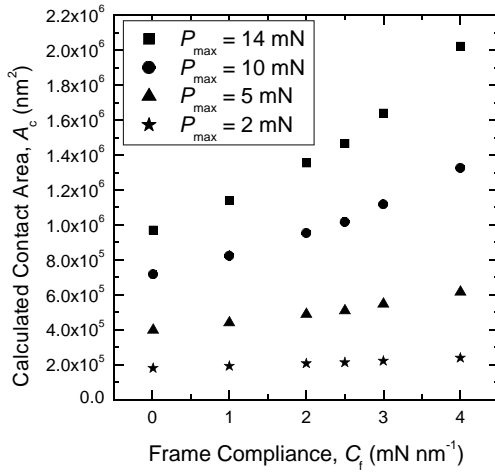


Figure 3-4: Calculated contact area (A_c) for fused silica data assuming different values of the frame compliance (C_f).

The combination of the data from Figures 3-3 (h_c) and 3-4 (A_c) gives the data which is used for fitting the calibration area function, as shown in Figure 3-5. An approximate area function fit is demonstrated here for each frame compliance level with quadratic polynomial fits (although no experimentalist would consider calculating an area function from data at only four different peak load levels!) Using these fits, the simple two-parameter paraboloid area function (Eqn 3-5) parameters C_0 and C_1 are themselves strong functions of frame compliance, as is obvious from the large differences in the quadratic fits in Figure 4. The direct dependence of these area function parameters (C_0, C_1) on the frame compliance (C_f) is shown in Figure 3-6.

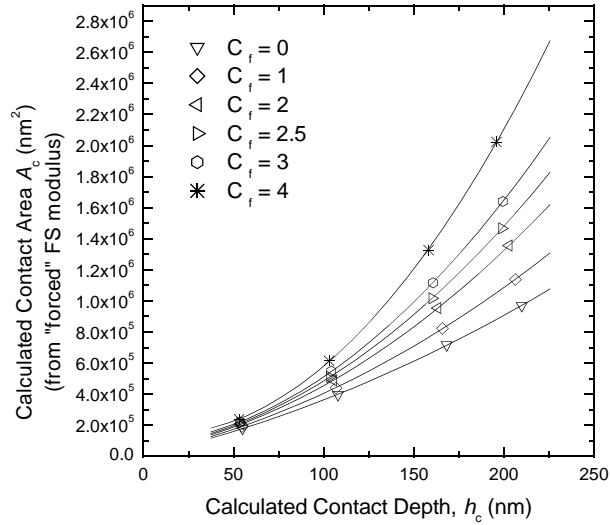


Figure 3-5; Hypothetical area function $A(h_c)$ fitting for different assumed values of frame compliance (C_f). Data are from Figures 3-3 and 3-4.

It is clear that for each different value of frame compliance that was assigned in the above data, a different area function was calculated for that frame compliance (Figure 3-5). Thus the full calibration can be thought of as the paired combination of a frame compliance value and a corresponding area function value. Since the area function is calculated by “forcing” the elastic modulus of fused silica is known and constant, any possible $C_f - A_c(h_c)$ combination results in data that give the apparently correct value of elastic modulus when the calibration pair is used on the fused silica data (the same data from which the calibration was performed) to calculate the elastic modulus and hardness as though the data were any arbitrary experimental data. This is demonstrated in Figure 3-7 (left). At depths of 50 nm and greater, the calculated (reduced) modulus is in approximately perfect agreement with the “known” value of 69.6 GPa for all assumed values of the frame compliance. (The low-depth data typically require some fine-tuning of the area function and, frequently, the addition of a third term to the area function.) Therefore the elastic modulus cannot be used to select the correct calibration. A second independent measurement is required to establish which of the calibration pairs

$(C_f - A_c(h_c))$ is the correct calibration. This is shown in Figure 3-7 (right) where the contact hardness value is only constant and correct for a single value of the frame compliance (here $\sim 2.5 \text{ nm mN}^{-1}$). An alternative (better) second measure of the correct area function-frame compliance calibration is a constant and numerically correct elastic modulus value for tests conducted on a second material.

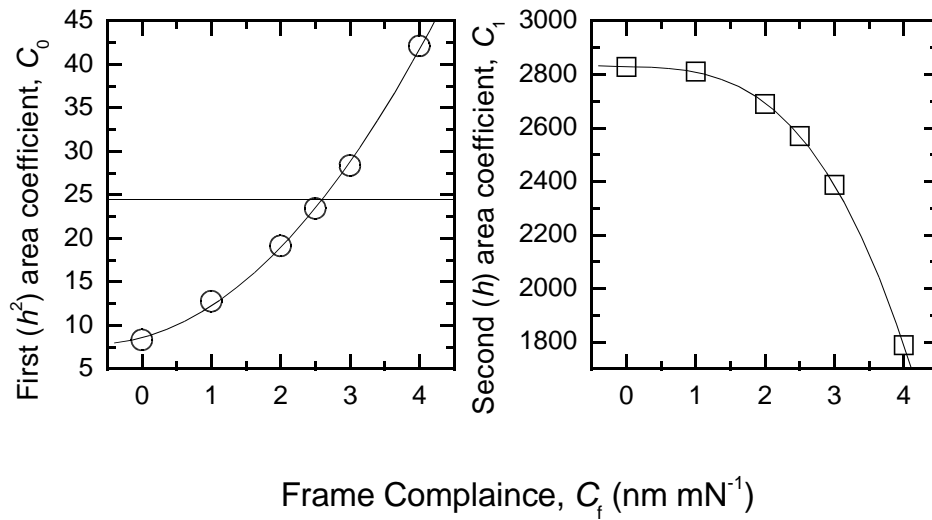


Figure 3-6: (left) First term of the calculated area function and its dependence on the assumed frame compliance value (C_f). The solid line is at the “perfect” value of 24.5. (right) Second term of the calculated area function and its dependence on the assumed frame compliance (C_f).

It is also interesting to note the strong dependence of the first term (C_0) of the area function on the frame compliance (Fig. 3-6). This number appears to provide a double-check of the correct calibration: if C_0 is substantially different than 24.5 (the predicted value for an ideal Berkovich indentation tip), something has gone wrong with the frame compliance calibration. This internal check of the area function leading term has worked well in the current system, in that the C_0 value is closest to 24.5 for $C_f = 2.5 \text{ nm/mN}$, the value in the chosen “correct” calibration pair (based on the contact hardness

data in Fig. 3-7). The correct frame compliance value can also be verified by making SEM measurements of the residual impressions [Doerner and Nix, 1986]. However, this exercise has demonstrated that it is crucially important to calculate the tip area calibration function in conjunction with the correct value of the frame compliance.

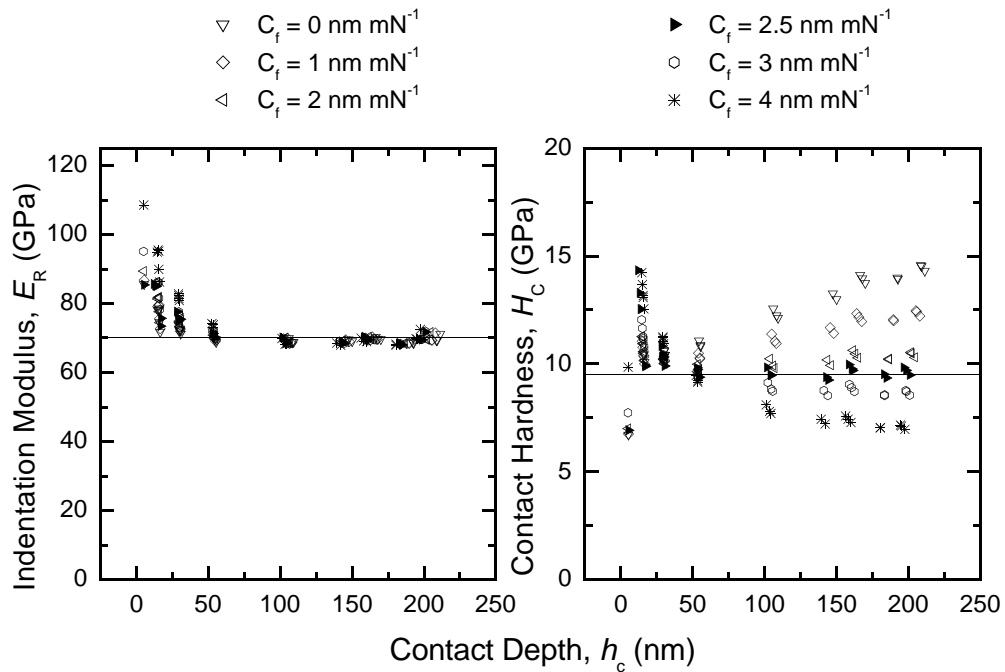


Figure 3-7: Calculated reduced modulus (E_R) and contact hardness (H_c) as a function of contact depth (h_c) for fused silica using calibration pairs with different assumed frame compliance values. The solid lines represent the approximate known values for E_R and H_c for fused silica (70 and 9.5 GPa, respectively).

3.1.2 Compliant Material Calibration Issues

Many questions regarding indentation calibration and data analysis have arisen as indentation testing has increasingly been performed on compliant polymer and biological materials (as opposed to the stiff engineering materials for which these nanoindentation instruments were designed and optimized). Two issues specifically relating to compliant

materials will be discussed in the following section: whether a different calibration protocol is required, and if there are issues with the fundamental contact mechanics used in Oliver-Pharr analysis that lead to systematic overestimates of the elastic modulus of compliant materials.

3.1.2.1 Calibration Standards for Compliant Materials

A question is raised when indentation testing is being performed on materials substantially more compliant than those typically used as calibration standards. For example, fused silica and aluminum both have elastic modulus values near 70 GPa, while most polymeric materials have modulus values around 5 GPa or (much) less, depending on the material and glass transition temperature. Bone and dentin have modulus values in the range from 10-30 GPa, which has resulted in discussion of potential alternative calibration standards for indentation of compliant materials [Chang et al, 2003b]. There is no widely accepted polymer standard for indenter tip calibration; a polymer would be extremely difficult to use as a standard due to the intrinsic time-dependence of the material and the effects of this time-dependence on indentation response (to be discussed further in Chapter 4).

As discussed above, the area function used to describe the tip-sample contact is typically described with the form of Eqn. 2-8, of which Eqn. 3-4 is a truncated form. For comparison of my own MTS-machine function I will include a third term here, such that the area function is:

$$A(h_c) = C_0 h_c^2 + C_1 h_c + C_2 h_c^{1/2} \quad [3-8]$$

This sum for the contact area is plotted in Figure 3-8 for approximate values of the calibration constants employed in the current work ($C_0 = 24.5$, $C_1 = 800$, $C_2 = 2000$) along with each term separately.

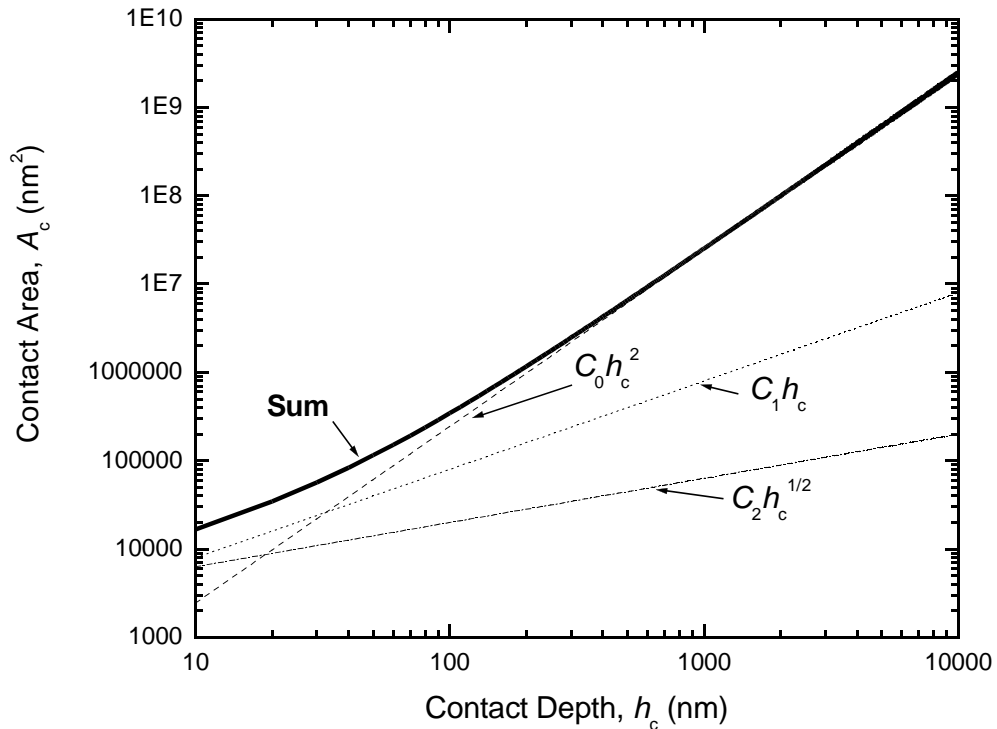


Figure 3-8: Plot of the complete area function $A(h_c)$ and the individual component terms (see Eqn. 3-8) for an experimentally-observed area function. The sum is influenced by the h and $h^{1/2}$ terms at small depths ($h_c < 200$ nm) but is dominated by the h^2 term at large depths.

As is apparent from the plot, the C_1 and C_2 terms are dominant at small contact displacements, but make almost no contribution to the sum at depths of about 200 nm and greater. Therefore, for indentation loads sufficiently large to cause the total indentation contact depth to be on the order of 1 μm or more, the first term of the area function is dominant in determining the contact area. The smaller the elastic modulus of the material, the larger the contact depth at fixed load, such that the odds of achieving an indentation depth of 1 μm or more at a reasonable (noise-free) nanoindentation load level are improved. However, it is useful to recall the differences in indentation displacement measurement hardware and ranges associated with different commercially-available indentation instruments (section 2.1.6 above); for large indentation depths ($> 2 \mu\text{m}$) the

Hysitron instruments are unsuitable.

From a tip calibration perspective, then, for compliant (and soft) materials it is important to determine an accurate value of the C_0 term in the tip area function since this is the only term that bears on the contact area calculation. However, a value of 23 or 26 for C_0 gives a calculated contact area only 6% different than that calculated for $C_0 = 24.5$! The implications for indentation of compliant materials are apparent: the choice of an idealized area function

$$A(h_c) = 24.5 h_c^2 \quad [3-9]$$

is acceptable for most testing, particularly for indentation depths of a micrometer or more.

3.1.2.2 Oliver-Pharr Analysis and the Contact Displacement

Although there is no question that the introduction of Oliver-Pharr analysis has made an enormous impact on mechanical testing in the last decade, the method itself is probably applied more broadly than is warranted. It has been noted that the indentation modulus of polymeric materials is frequently larger than the modulus of the same materials measured in uniaxial tension or compression [Moody et al, 2002]. The modulus is also frequently not constant, as shown below in Figure 3-9 for Berkovich indentation of PL-1 polymer using the CSM technique (section 2.1.6.1) to record modulus as a function of depth. The dashed line is the known elastic modulus of the material (provided by the manufacturer, Measurements Group, Raleigh, NC) after conversion from plane strain modulus using the known value of Poisson's ratio (ν). Even at depths of more than 5 μm the CSM (indentation) modulus is larger than the elastic modulus measured in tension.

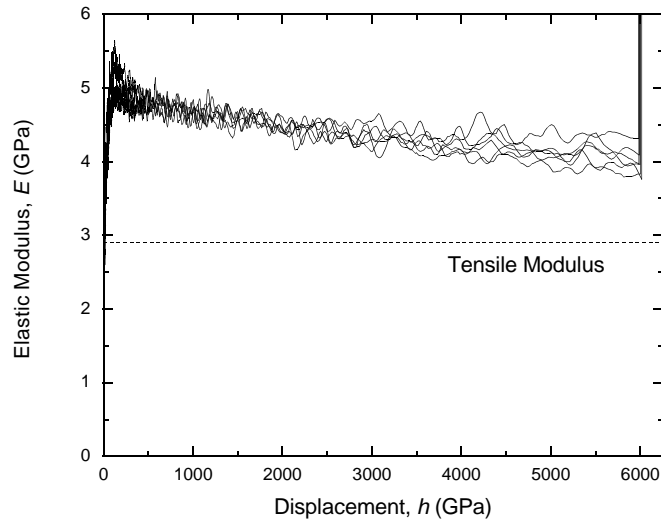


Figure 3-9: Depth-dependence of the elastic modulus (E) of a polymer (PL-1) as measured by nanoindentation. The dashed line (2.9 GPa) is the approximate tensile modulus of the polymer, demonstrating the modulus overestimation frequently associated with conical-pyramidal nanoindentation.

There are both physical and mechanical factors that could be implicated in this discrepancy between indentation and homogeneous modulus measurements:

- physical aging of the polymer surface due to oxidation or other chemical mechanisms could be associated with changes in the surface mechanical properties, and those, rather than the bulk values, are the properties which are measured by nanoindentation
- time-dependence in the polymer mechanical response could be affecting measurements (this will be addressed in detail in Chapter 4)
- effects such as “pile-up” and “sink-in” which are associated with plasticity and cause errors in the estimation of contact depth, h_c , from displacement, h . (This topic has been previously discussed in indentation analysis of elastic-plastic systems, particularly in the context of work-hardening metals [Cheng and Cheng, 2004])

To address this last point within the context of polymers, an examination of the contact depth h_c , and how this differs from the total displacement, h is needed. The elastic solution for conical indentation gives:

$$P = \frac{\pi \tan \psi}{2\gamma^2} \frac{E}{(1-\nu^2)} h^2 \quad [3-10]$$

where the factor γ relates the contact depth (h_c) to the total displacement (h):

$$\gamma = \frac{h}{h_c} = \frac{\pi}{2} \quad [3-11]$$

for an elastic half-space [Sneddon, 1965]. For purely elastic indentation, Eqn. 3-10 can be used to directly fit the indentation data and estimate the elastic modulus. However, as demonstrated in chapter 2, there is substantial plastic deformation associated with pointed indenter tips, such that the elastic displacement is not known independently and the Oliver-Pharr calculation of h_c is done using the peak load and unloading stiffness (P_{\max}, S) to estimate the elastic displacement, since the indentations are elastic-plastic, not elastic; the factor γ is embedded in this analysis and is fixed at $\gamma = \pi/2$. If the value of γ present during the elastic-plastic experiment was substantially different than the known elastic value, this would appear as an error in the perceived elastic modulus of the material as measured using Oliver-Pharr analysis.

In elastic-plastic indentation experiments, it has been noted both by direct measurement and by finite element calculations that the experimental value of γ may in fact differ from $\pi/2$. It has been noted [Thurn et al, 2002] that experimentally measured γ was closest to ideal ($\pi/2 = 1.57$) for extremely stiff sapphire ($E \sim 440$ GPa), and then decreased for materials with smaller modulus (stiffness) values. The γ value was about 0.9 for NaCl, which has modulus of ~ 38 GPa. A similar finding was reported for

amorphous Selenium [Shimizu et al, 1999] in which the authors concluded that experimentally the value of γ is approximately unity.

There are two ways that a material with $\gamma \neq \pi/2$ could cause problems in quantitative nanoindentation measurements. First, calibration of the tip area function requires a “well-behaved” material with a γ of $\pi/2$. It is partly for this reason that calibrations are undertaken using stiff glass and ceramic materials as the calibration standards. The use of a calibration material with an unexpected γ , as in many soft metals and polymers, would result in numerical errors in the area function when attempting to then use this area function to measure properties in a material with the correct γ . Attempts to “force” the area function to conform to a uniaxial tension elastic modulus [Chang et al, 2003b] are intrinsically error-ridden, due to time-dependence in the polymer and the outstanding lack of certainty associated with the overestimation of polymer modulus values frequently observed. This topic will also be further discussed in section 3.2.2 below, in which the data published previously with a forced polymer-based area function are corrected and found to be in agreement with the existing literature and independent measurements using the same sample and a different indentation instrument.

Since calibrations are typically carried out with stiff glass and ceramic materials, this issue would help explain why the Oliver-Pharr modulus values for many polymers, even after accounting for time-dependent effects, are overestimated in nanoindentation. An alternative model for time-dependent indentation data analysis, in which γ is taken to be 1, results in modulus values closer to the known modulus for polymers such as PL-1 (Figure 4-15). This model (and these PL-1 polymer data) will be discussed later, within the context of time-dependence in Chapter 4. It is interesting to note, however, that the difference in modulus values obtained at different depths remains.

The deviation of γ from $\pi/2$ is theoretically not due to viscoelastic effects. It has been shown that the elastic γ is equally applicable to viscoelastic problems, and this has been confirmed by recent finite element analysis on conical indentation in a viscoelastic medium [Cheng and Cheng, 2004]. However, problems with γ arise in elastic-plastic

deformation due to the plastic component of the deformation, and therefore the same plastic-based issues with this factor could arise in viscous-elastic-plastic problems.

3.2 Elastic-Plastic Bone Indentation

Having critically examined indentation calibration and issues for compliant materials, the technique will be applied (using Oliver-Pharr analysis) to elastic-plastic indentation testing and analysis on mineralized tissues, mainly bone. A brief overview of a large healing bone study, from which samples will be used in several different portions of this work, is presented.

3.2.1 Bone-Dental Implant Study Methods

Healing bone samples adjacent to a dental implant interface were the focus of several aspects of the current work, as well as one previously published study [Chang et al, 2003b]. In the study, the 4th premolars of six 2-year-old Sinclair miniswine were unilaterally removed surgically and a titanium dental implant was inserted in the alveolar ridge seven months after the extraction. The implants were shielded from bite forces and left in place for one month (two animals), two months (two animals) or four months (two animals) prior to animal sacrifice. Three bone samples adjacent to the screw-implant (Figure 3-10) were harvested embedded in polymer resin (PL-1, Vishay Micro-Measurements, Raleigh, NC). The samples were sectioned 1-2 mm thick, and sequentially polished to 0.05 μm using standard metallographic techniques, to prepare the surfaces for indentation testing. The samples were stored frozen until indentation testing was performed, and returned to the freezer between studies.

Different groupings of these same samples will be examined in portions of the current work:

- i. In section 3.2.2, one-month healing samples indented with two different instruments will be compared. The original (Hysitron) study uses samples 1-3 of both one months animals and was published previously [Chang et al, 2003b]; the original result appears in Figure 3-11. The data were re-analyzed following calibration and compared with new experiments using the MTS instrument. The new MTS study uses one sample

each from the two animals at one month healing time, sample (1) from one animal and sample (2) from the other.

- ii. In section 3.2.3, all samples (1)-(3) at all healing time points (1, 2, 4 months) are examined after recalculating the data following the recalibration discussed above in part (i). The original experiments were performed on the Hysitron instrument.
- iii. In section 3.3.2, one sample (1) from one month healing (as used in part (i)) is used to demonstrate load-dependent indentation variability
- iv. In section 3.4.2, the (1) sample from one animal each at one, two and four months is used to demonstrate nanoindentation modulus mapping in two dimensions. The 1-month specimen used is different than those used in parts (i) and (iii) of this listing.
- v. In section 4.1.2 the time-dependence of indentation responses in a 2-month (1) sample are demonstrated. This is the same sample as in part (iv) of this listing.
- vi. In section 4.4.2 the MTS experiments from part (i) of this list are re-examined within a time-dependent indentation framework. Further analysis of this same experiment appears in sections 4.4.3 and 4.5.3.

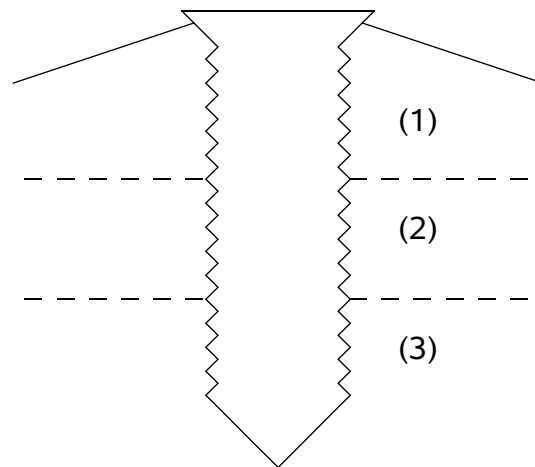


Figure 3-10: Three bone samples, designated (1)-(3), were harvested from bone along the dental implant interface for each animal.

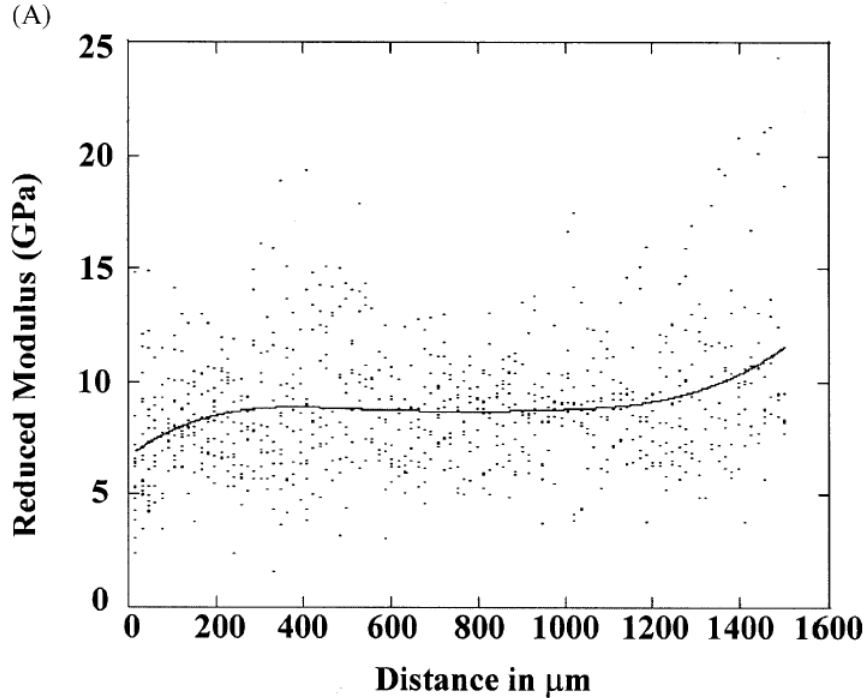


Figure 3-11: Plane strain modulus (E') vs distance from the bone-implant interface for one month healing [from Chang et al, 2003b]

3.2.2 Effect of Instrument and Calibration

It became of practical interest to verify that there was no possibility for machine-based and calibration-based differences in indentation elastic-plastic mechanical properties obtained using different nanoindentation instruments. The mineralized tissue nanoindentation studies (performed by myself) reported in the current work were done using an MTS Nanoindenter XP instrument. Indentation tests on the same series of bone samples were done previously with a Hysitron Triboscope and preliminary results for one month bone healing were published [Chang et al, 2003b]. In the published study, a novel polymer-based indenter tip calibration was used along with the Hysitron instrument.

Values for the indentation modulus and contact hardness in porcine healing bone (reported in [Cheng et al, 2003b]) were at the extreme low end of the range of values previously seen in other bone indentation studies [Turner et al, 1999; Zysset et al, 1999].

For example, the average modulus value in Cheng et al was 8.4 GPa, and the average contact hardness was 0.2 GPa. Elastic modulus values for dry human cortical and trabecular bone ranged from 16 to 24 GPa in one nanoindentation study [Turner et al, 1999]. Contact hardness values for wet human bone ranged from 0.23 to 0.76 in another study [Zysset et al, 1999] and in this same study modulus values ranged from 7 to 25 GPa. Several differences were present between these sets of data, including the bone source species, indentation instrument and testing conditions. It was desirable to eliminate the potential for machine- and calibration-based differences between the protocols in order to establish if the lower modulus and contact hardness values seen in Chang et al [2003b] were due to the bone status, species, or other unknown differences.

A series of indentation tests were performed on two bone samples with 1-month healing time, using the MTS Nanoindenter XP instrument. Indentation loads were comparable to those used in the original study (6 mN for Hysitron vs 10 mN for MTS) although spacing between individual indentation tests was different (15 μm spacings for the Hysitron, $\sim 100 \mu\text{m}$ spacings for the MTS). The bone samples were tested dry instead of hydrated, as there is no easy mechanism for sample submersion on the base model NanoIndenter XP. (Samples were soaked prior to Hysitron testing in the original study but were not kept submerged; there was in fact potential for evaporation and dehydration during the test.) The average experimental modulus for the new data (obtained using Oliver-Pharr deconvolution) was found to be 17.9 GPa and the average contact hardness was 0.5 GPa. The effect of hydration in bone indentation testing has been documented at 25% [Rho et al, 1997; Ferguson et al, 2003], and thus could not explain the factor of approximately two in the comparison of the published data with the current study. The Hysitron data were therefore examined more carefully.

The polymer-based calibration protocol used in the original (Hysitron) study [Cheng et al, 2003b] could not be eliminated as a potential factor in this large difference, nor could improperly set values of the frame compliance. As was discussed in section 3.1.2.2 above, the modulus of polymeric materials is frequently overestimated using nanoindentation techniques. Therefore, “forcing” a modulus value for a polymer

(as was done in the original Cheng et al study) would result in dramatic overestimation of the contact area, which in turn would result in underestimated numerical values for E' and H_c when testing unknown samples.

After re-calibrating the indentation tip area function using the standard calibration protocol and modulus “forcing” to fused silica values (as per section 3.1.1 above) the Hysitron data for bone with 1-month healing was found to have an average modulus value of $E' = 12.9$ GPa, $H_c = 0.4$ GPa, much closer to previously published values for bone [Turner et al, 1999; Zysset et al, 1999]. The old (e.g. From Fig. 3-11 as originally published) vs new (recalculated after the recalibration) modulus values for the Hysitron experiment 1-month healing data are shown in Figure 3-12 below. Not only did the average increase by about 50%, but the range of experienced values increased (20 compared to 12 GPa), again in better agreement with other experiments published previously on hydrated bone [Zysset et al, 1999].

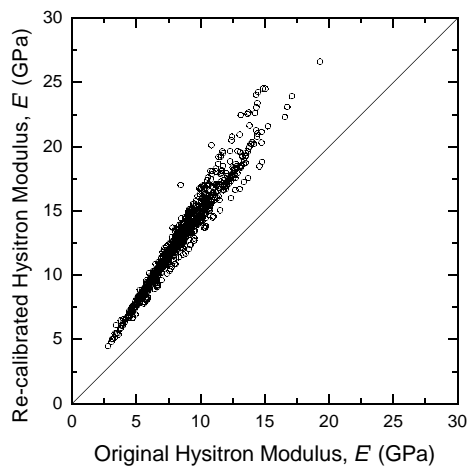


Figure 3-12: Plot of 1-month healing bone plane strain modulus (E') from the original indentation study (Figure 3-11) versus modulus following re-calibration of the Hysitron instrument tip area function. Both the numerical values themselves and the range of observed values increased as a result of the calibration.

The recalibrated modulus data from Figure 3-12 is shown as a function of distance from the bone-implant interface in Figure 3-13. The data from the new MTS experiments

on the same samples are also shown in Figure 3-13 (left) and the modulus values are larger on average (MTS: $E' = 17.9 \pm 4.4$ GPa; Hysitron: $E' = 12.9 \pm 3.6$ GPa). However, if the MTS modulus values are decreased by 25%, to approximate the effect of dry vs wet samples [Rho et al, 1997], the data are approximately equal in average (MTS adjusted for hydration $E' = 13.4$ GPa) and overlap on the plot versus distance (Figure 3-13, right). The scatter in values is approximately the same for both machines as well.

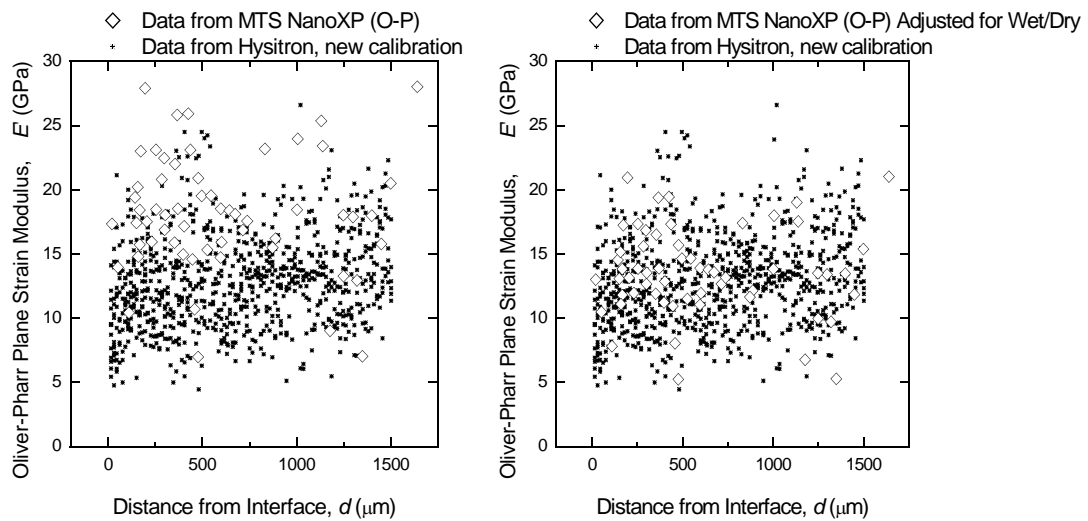


Figure 3-13: (left) Plot of plane strain modulus (E') versus distance from the bone-implant interface for the same 1 month bone samples tested with a Hysitron instrument (peak load 6 mN, Figure 3-11) and an MTS instrument (peak load 10 mN). (right) same data after MTS machine values were scaled to 75% their original values to approximate a change from dry to wet testing conditions. Experimental data from the two machines now agree well both in value and in scatter.

This result clears the way for further studies of these samples using the MTS instrument, in that the results appear to be quantitative and in agreement with the previous study. In addition, the Hysitron results will be re-analyzed with the new calibration and examined for comparison with the new (MTS) studies.

3.2.3 Effect of Bone Healing Time

The newly calibrated tip area function was used to re-analyze the Hysitron indentation data for porcine bone at healing times of 1-, 2-, and 4-months post-implant (These original indentation experiments were performed previously by C-C Andy Liu but are presented here following this crucial re-calibration for comparison with the new MTS experiments done on the same samples later in this chapter.) Modulus data showed substantial scatter (Figure 3-14) and a subtle trend towards increasing modulus with increased distance (d) from the bone-implant interface. The contact hardness data showed a similarly large degree of variability and a similar, perhaps even subtler, trend with respect to distance from the implant interface (plot not shown).

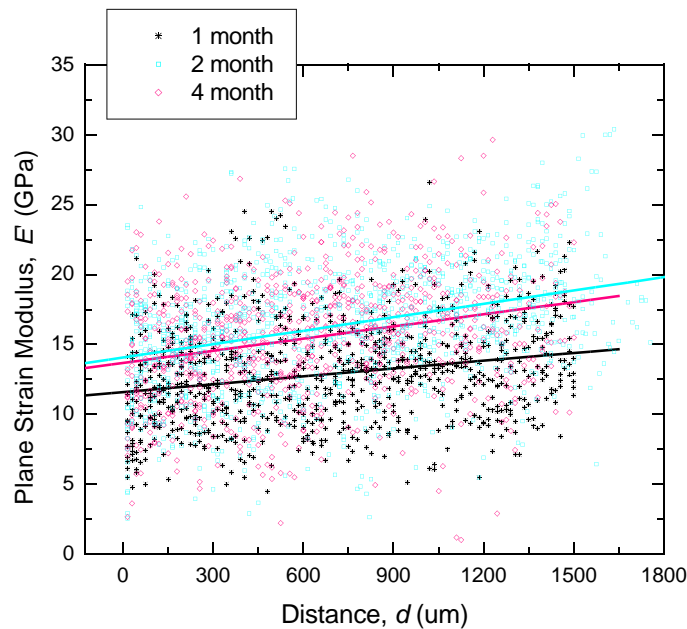


Figure 3-14: Plot of modulus (E') versus distance from the bone-implant interface for Hysitron indentation tests at 1, 2, and 4 months. The scatter is large, slightly obscuring the apparent trend toward increased modulus at greater distance from the interface. The trend lines for each data set are shown.

These data demonstrate a slight increase in both plane strain modulus and contact

hardness for four month healing compared to one month healing (Table 3-1). The data for two month healing appear to be, on average, even greater than those for four month healing.

Table 3-1: Mean values and standard deviations for plane strain modulus (E') and contact hardness (H_c) at one, two and four months bone healing time.

<i>Healing Time</i>	<i>Plane Strain Modulus, E' (GPa)</i>	<i>Contact Hardness, H_c (GPa)</i>
1 month	12.9 ± 3.6	0.41 ± 0.14
2 months	16.3 ± 4.4	0.55 ± 0.16
4 months	15.5 ± 4.3	0.48 ± 0.14

Statistically, because of the extremely large number of individual test values (more than 500 individual indentations for each time-point), the data in Table 3-1 are all significantly different by one-way ANOVA with multiple comparisons (with the factor of healing time). However, it would be very difficult to defend the differences as physically significant, given the large standard deviations and large scatter in the measurements.

Histograms were generated for the modulus data shown in Figure 3-14 to examine the distribution of modulus values as a function of healing time. The modulus values were found to vary widely in these experiments, but were approximately normally distributed (Figure 3-15).

Based on the wide variation seen in these results, any trend in healing bone with either time (1, 2, 4 months healing) or distance (d) from the implant interface is to some degree obscured by the substantial variability in point to point mechanical properties obtained via indentation testing. It was hypothesized, based on these results at 6 mN peak load, that the indentation responses were variable due to the small length-scales of the indentation test relative to the ultrastructure of the bone tissue itself. Therefore an examination of load-level (and in term length-scale) variability in indentation of mineralized tissues composites was undertaken.

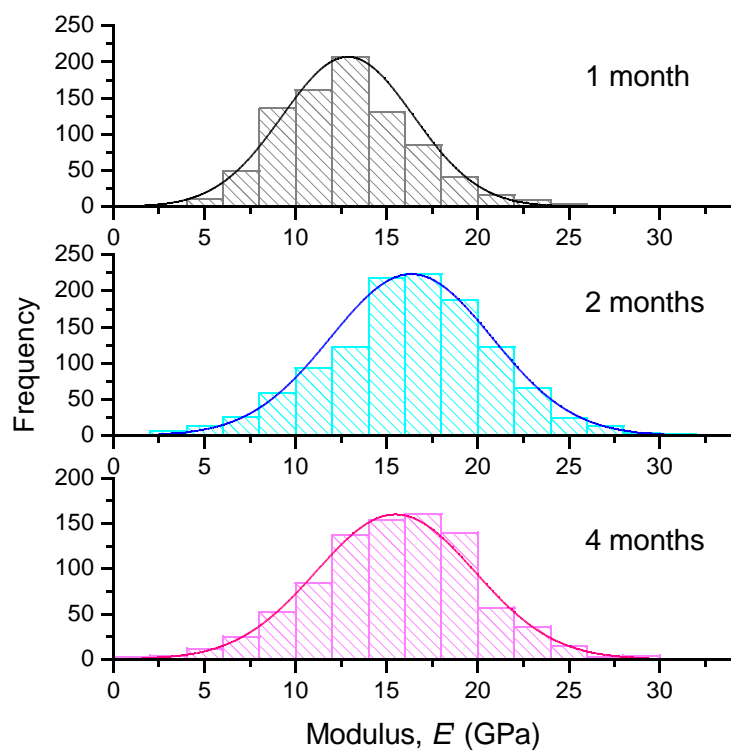


Figure 3-15: Frequency histograms for modulus (E') values at different time points after bone healing for 1, 2, and 4 months.

3.3 Nanoindentation Variability Experiments

Large variability was seen in the bone indentation experiments presented in the previous section. The indentation tests in that experiment were conducted at 6 mN. It was desired to examine the variability in bone and related materials as a function of indentation peak load level, to try and eliminate sources of experimental variability due to the selection of testing parameters and establish a continuum-level single-valued elastic modulus for the composite materials being examined. Indentation experiments were thus conducted over a range of peak load levels on homogeneous materials and on natural mineralized nanocomposite materials.

3.3.1 Homogeneous Controls

Experiments were performed to examine local length-scale effects in nanoindentation. First, smooth and homogeneous fused silica (the calibration standard) was used as a control to establish the potential magnitude of artifacts such as instrumentation variation at different length-scales and the effect of sample preparation, particularly the polishing of the surface.

Nanoindentation tests were performed on an MTS Nanoindenter XP (MTS Systems Corp., Eden Prairie, MN) with a Berkovich pyramidal tip. Single load-unload triangle-wave loading cycles were performed using constant loading-rate tests to peak loads of 1, 10, and 100 mN at a fixed rise time of 30 seconds (8 tests per peak load). Plane strain modulus (E') was deconvoluted from load-displacement responses using typical elastic-plastic techniques [Oliver and Pharr, 1992].

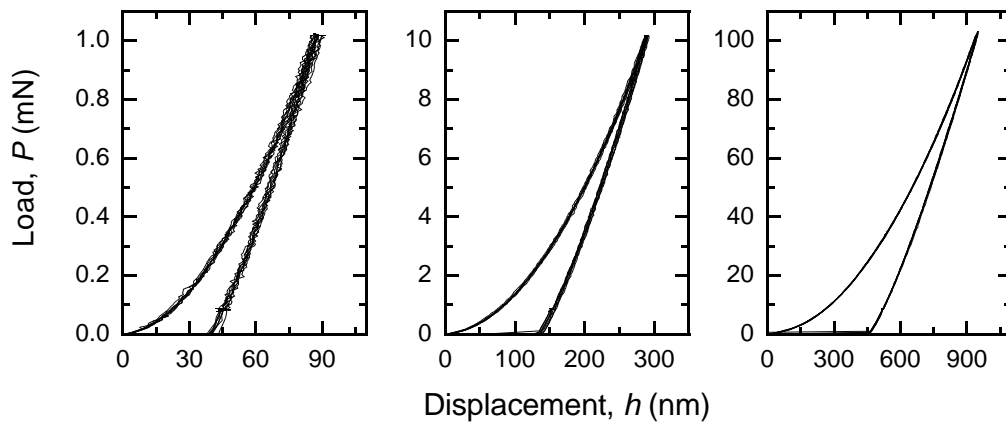


Figure 3-16: Raw indentation load-displacement (P - h) responses for fused silica tested at three different peak load levels.

The raw load-displacement (P - h) traces for the fused silica indentation tests at 1, 10, and 100 mN are shown in Figure 3-16. Two things are immediately apparent from the data: the shape of the response is conserved at different peak load levels, due to the effect of geometric similarity of the Berkovich indenter tip, and the responses superpose and demonstrate little variability at any load level. This is reflected in the modulus data deconvoluted from the traces using Oliver-Pharr analysis; the modulus data are constant in value and show little variability in terms of total range of values (Figure 3-17). The diminishing range of modulus values with increasing indentation peak load level is reflected in the raw data in Figure 3-16 in that the line widths used in the plots were identical so the broader lines at 1 mN reflect small variations in the responses. These data have been plotted with an elastic modulus range of one order of magnitude, for comparisons of the variability in responses for materials with different baseline elastic modulus values in the following sections.

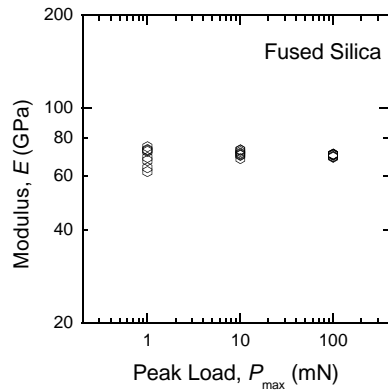


Figure 3-17: Elastic modulus (E) data (from Oliver-Pharr deconvolution) as a function of indentation peak load (P_{max}) for for the fused silica indentation tests shown in Figure 3-16. Modulus values for each individual test are shown as a single point in the plot.

A second homogeneous control with direct relevance to the current study was examined. Single-crystal (gem-quality) mineral apatite (fluoroapatite) was also acquired (Marin Mineral Company, sample obtained from Cerro de Mercado, Durango, Mexico). The sample was sectioned and polished for indentation analysis. Modulus data as a function of indentation peak load are shown in Figure 3-18.

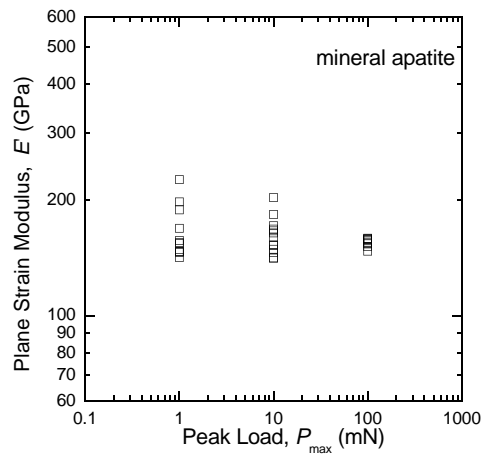


Figure 3-18: Plane-strain modulus (E') data (from Oliver-Pharr deconvolution) as a function of indentation peak load (P_{max}) for single crystal mineral apatite

3.3.2 Biological Composites

Mineralized composite biological tissues were next examined within this framework of indentation length-scale variability. Porcine bone samples were used, as described in section 3.2.1; indentation tests were located on the alveolar cortical bone. Tooth cross-sections were made by sectioning extracted 3rd molars in the transverse plane to expose dentin and enamel, and wet-polishing the surface in a manner similar to that used for the bone samples discussed in section 3.2 above. All bone and tooth samples were stored frozen until testing and were tested in ambient conditions (*e.g.* dehydrated).

Elastic plane strain modulus-indentation peak load (E' - P_{\max}) data is shown in Figure 3-19 for bone and in Figure 3-20 for the mineralized tooth tissues. Interestingly, considering the similarities in composition for bone and dentin, there was a substantial difference in the degree of variability seen in the indentation responses. The enamel was even less variable than the dentin at small depths.

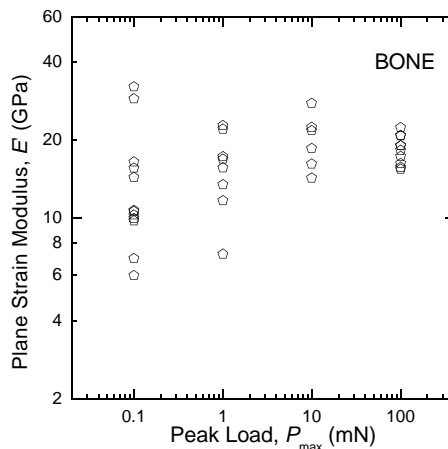


Figure 3-19: Variability in bone indentation modulus (E') at different peak load levels (P_{\max}).

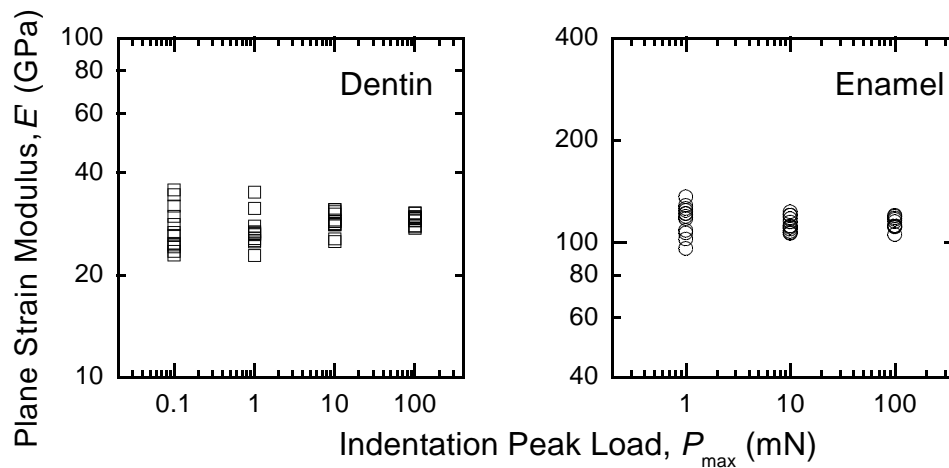


Figure 3-20: In contrast to bone (Fig. 3-19 above) there is relatively little variability in indentation modulus (E') of mineralized tooth tissues tested at different peak load levels (P_{\max}).

3.3.3 Summary of Indentation Variability

Indentation responses of homogeneous materials, fused silica glass and mineral gem-quality apatite, were uniform even at very small indentation peak load levels and depths (Figures 3-17 and 3-18). Interestingly, the composite materials in tooth, dentin and enamel, are also relatively uniform in response, even at small indentation length scales (Figure 3-20). The bone samples, in contrast, were variable at all peak load levels (Figure 3-19).

The data in Figures 3-17 to 3-20 are tabulated for quantitative analysis in Tables 3-2 for small load levels and 3.3 for large load levels. The mean and standard deviations are used to calculate the relative variation (coefficient of variation, COV) for each material at small and large load levels. Several interesting trends emerge from this calculation. At small load levels, for homogeneous materials (fused silica and mineral apatite) there is a degree of intrinsic variability, attributable to the instrumentation at such small (nm) length-scales. Interestingly, the data for biological composite tooth tissues

are comparable in variability to the homogeneous materials at both small (Table 3-2) and large (Table 3-3) load levels.

There was a dramatic variability in the bone data for variability, both at small indentation loads (Table 3-2) and at larger indentation loads (Table 3-3), such that the bone tissues were uniquely and substantially variable at all length scales tested. The bone variability can therefore be considered “real” and not due to artifacts of machine (by comparison with homogeneous materials) or of sample preparation (by comparison with similarly-prepared tooth tissues).

Table 3-2: Small-depth ($P_{\max} = 0.1$ or 1 mN) indentation modulus variability (data from plots 3-17 to 3-20)

	<i>*Peak Load level, P_{\max} and mean peak depth, h_{\max}</i>	<i>Mean Plane Strain Modulus, (\bar{E}')</i>	<i>Standard deviation (SD)</i>	<i>Percent Coefficient of Variation 100 % \bar{E}'/SD</i>
Fused Silica	1 mN 87 nm	69.39	4.64	6.7
Mineral apatite	1 mN 71 nm	166.28	26.84	16.1
Enamel	1 mN 90 nm	117.06	11.75	10.0
Bone	0.1 mN 131 nm	14.32	8.23	57.5
Dentin	0.1 mN 62 nm	27.76	4.33	15.6

** peak load levels differed for the different materials to keep the mean peak depths approximately equal—since the tests are carried out in load-control, the peak depth at fixed load level is smaller for stiffer materials*

Table 3-3: Large-depth ($P_{\max} = 100$ mN) indentation modulus convergence for variability studies (data from plots 3-17 to 3-20)

	<i>Mean Plane Strain Modulus, (\bar{E}')</i>	<i>Standard deviation (SD)</i>	<i>Percent Coefficient of Variation 100% \bar{E}'/SD</i>
Fused Silica	70.04	0.65	0.93
Mineral apatite	155.25	3.73	2.4
Enamel	113.83	4.58	4.0
Bone	18.51	2.36	12.7
Dentin	29.15	0.94	3.2

Based on the similarities in composition between dentin and bone, it is a bit puzzling that the results are so dramatically different. The result directly implicates local structure and organization of the mineral phase as being different in bone and dentin, as will be discussed further in later chapters of this work. However, regardless of the source of the variability, the implications of this experiment are quite clear. Due to the dramatic scale of indentation variability in bone, clearly tests should not be performed at small indentation loads or length-scales. In fact, based on the diminishing variability of bone with increasing indentation load level (and corresponding increased length-scale), indentation measurements in bone should be carried out at load levels as large as is practicable.

3.4 Property Mapping

Having demonstrated in many different ways that the indentation responses of bone are variable, especially at small loads, a new technique was developed to map out material properties across a sample and allow for correlation of properties with microstructural features. The indentation experiments were performed at large peak loads ($P_{\max} = 100$ mN) to minimize any variability effects due to surface preparation, individual discrete elements such as mineral particles, and to try to obtain a near-continuum mechanical response for each location. The mapping experiments were performed on a tooth cross section, as a control to establish the technique, as well as three bone samples (one each for one, two, and four months healing time as discussed in section 3.2.1). The bone and tooth samples underwent identical sample preparation, storage, and testing protocols.

3.4.1 Mapping the Dentin-Enamel Junction

The dentin-enamel junction is an abrupt transitional region between two tissues with dissimilar compositions and elastic modulus values. Therefore, this DEJ region was used as a control to establish a technique of quantitative elastic modulus mapping via indentation testing. Crucial to this mapping technique is the registration of optical and mechanical information on the same composite image.

Fourteen lines of indentation tests were conducted across the DEJ in one quadrant of single tooth cross-sectional sample (Figure 3-21). Indent spacings were 100 μm in the x-direction (approximately perpendicular to the DEJ) and 100-200 μm in the y-direction (between lines of indents). Indentation conditions were peak load $P_{\max} = 100$ mN and $t_R = 33$ seconds (rate $k = 3$ mN s⁻¹). Optical images (160 x 120 pixels, corresponding to a sample region 600 μm by 400 μm) of the indented regions were captured in situ (following the indentation tests) and indenter stage coordinates were recorded for each

captured image. Adobe Photoshop “photomerge” feature was used to join the captured images into a single optical micrograph image of the indented region (Figure 3-22).

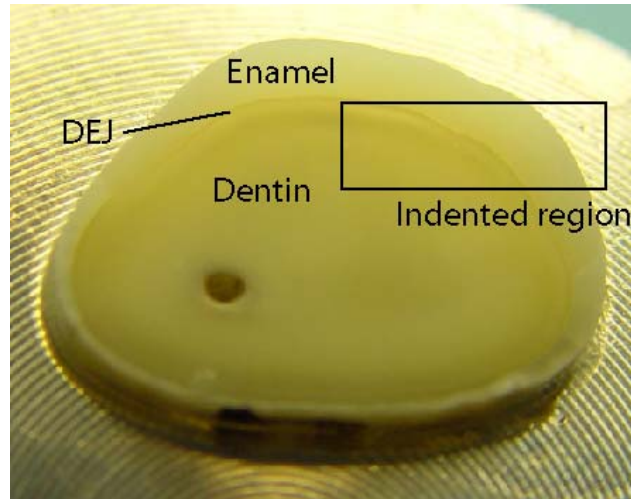


Figure 3-21 Cross section photograph of a tooth (3rd molar) illustrating the indented region of the dentin-DEJ-enamel transition region. The dentin and enamel tissues are clearly differentiable by color but the sample is otherwise featureless and homogeneous in appearance.

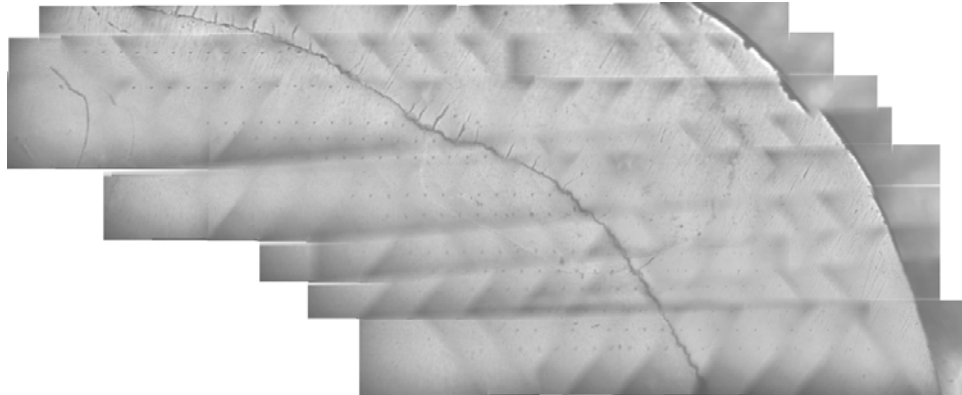


Figure 3-22: Composite image of the indented area, constructed from 130 overlapping images obtained through the nanoindenter positioning optics. Interference fringes are visible in this composite image due to the relative lack of features in the images, and thus the difficulty registering the images precisely.

Raw indentation load-displacement ($P-h$) traces for one (x -direction) row of indentation tests are shown in Figure 3-23. The data can be clearly grouped and identified as indentation tests on dentin and enamel. There is more variation in the dentin

responses than in the enamel responses, but not much variation in either set of indentation curves.

Indentation plane strain elastic modulus, obtained via Oliver-Pharr elastic-plastic analysis, was plotted as a map in two dimensions (Figures 3-24). The map was colored for easier viewing and matched to the optical composite image (Figure 3-22) using the stage coordinates for the collected optical images and indentation tests. The visible residual indentation impressions in dentin also assisted in verification of the registry of optical and mechanical images. The optical-mechanical map, consisting of the modulus mapped onto the optical image of the sample, is shown in Figure 3-25.

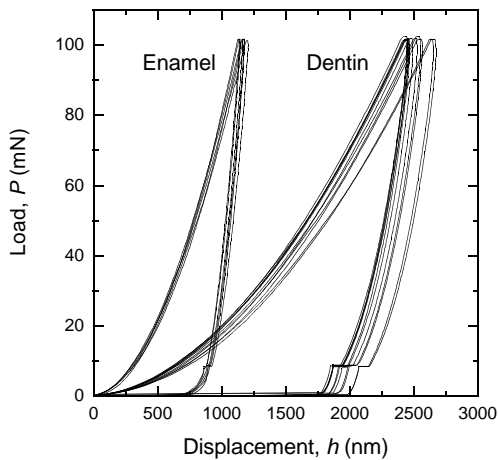


Figure 3-23: Raw indentation load-displacement (P - h) traces for one row (x -direction line) of indentation tests performed across the dentin enamel junction.

The elastic modulus maps illustrate clear differences between the dentin and enamel (Figures 3-24 and 3-25). An intermediate zone lying directly on the DEJ showed modulus values intermediate to the dentin and enamel values; these values likely reflect the indenter tip physically touching both tissue types as they are located directly on the boundary (Figure 3-25). A near-junction region, with slightly depressed elastic modulus values in the indents closest to the DEJ, was also observed in the dentin (most clearly visible in the composite image, Figure 3-25).

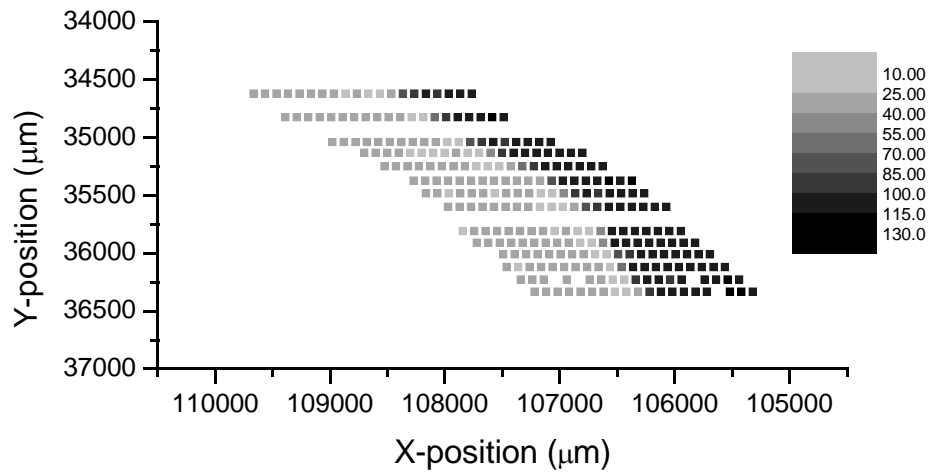


Figure 3-24 Plane strain elastic modulus (E') map of the dentin-enamel junction. Each colored square corresponds to the modulus value from one indentation test performed in that location. The dentin is clearly distinguishable from the enamel.

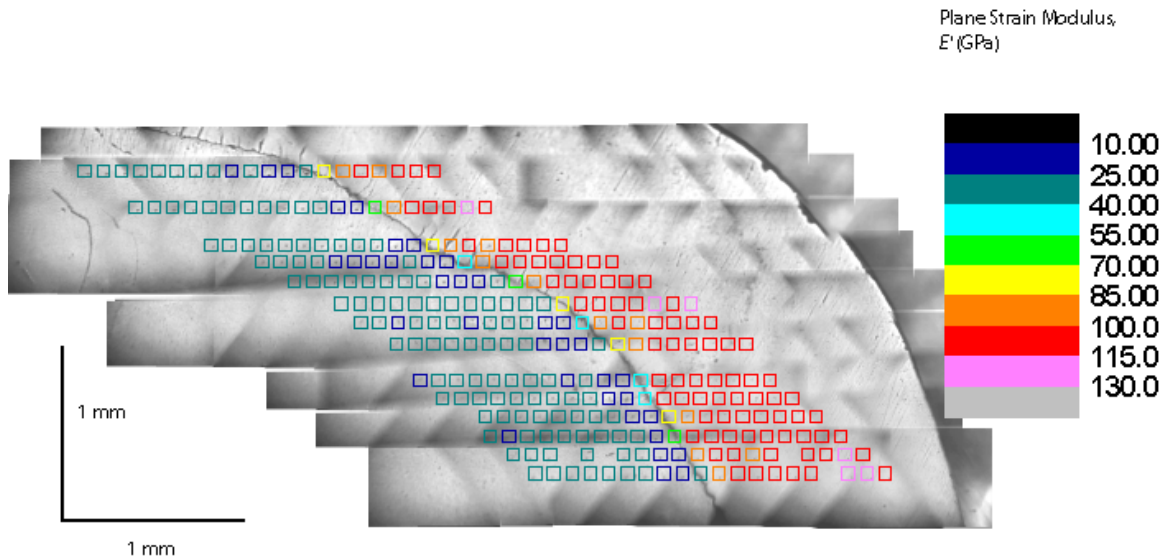


Figure 3-25 Plane strain elastic modulus (E') overlay map of the dentin-enamel junction. The modulus information from Figure 3-24 has been converted to color (for easier viewing) and mapped onto the composite image of the DEJ (Fig. 3-22) using the indentation residual impressions to match the images.

Having developed a technique for modulus mapping, and illustrating its use on a reasonably well-understood structure, the technique will next be applied to the analysis of bone tissues in the region near a bone-implant interface. This technique is advantageous in that the mechanical information and optical images are collected together, using a single set of physical stage coordinates from the indentation device (an MTS NanoXP, in this case), to allow for accurate placement of the indentation mechanical properties data on the corresponding optical composite image of the tissue, as was demonstrated above for the DEJ.

3.4.2 Bone Modulus Mapping

To assess spatial variation in healing bone mechanical response, arrays of indentation tests were run on the healing bone samples discussed above (section 3.2.1) and in Chang et al [2003b]. Elastic modulus was mapped over a large region of three samples, one each for one, two and four months bone healing time following implantation of a dental implant. The indentation arrays were rectangles with inter-indent spacings of 100 μm in both the x - and y - directions. Total array sizes were no smaller than 1.2 mm by 1.2 mm and originated along the bone-implant interface. Indentation conditions were peak load $P_{\text{max}} = 100 \text{ mN}$ and $t_{\text{RISE}} = 33$ seconds (loading rate $k = 3 \text{ mN s}^{-1}$).

Raw load-displacement (P - h) responses for a single row of indentation tests on one sample are presented in Figure 3-26. The data show substantial variability, in stark contrast to the comparable data shown for dentin (Fig. 3-23).

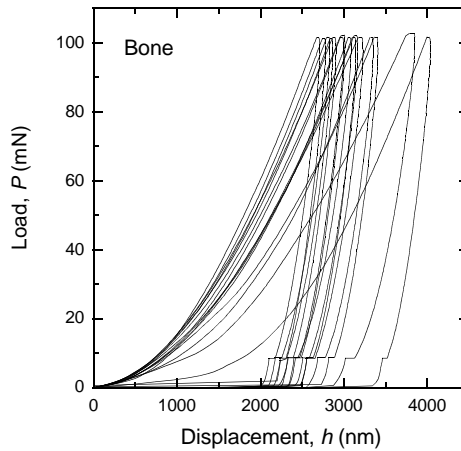


Figure 3-26: Raw indentation load-displacement (P - h) traces for one row (x-direction line) of indentation tests performed on a healing bone sample.

The procedure for generating the optical-mechanical maps was identical to that done for the DEJ (section 3.4.1 above): optical images of the indented regions captured *in situ* were used to generate a composite image of the indented region. Indentation elastic modulus (obtained via Oliver-Pharr analysis) was mapped onto the optical images. For each experimental specimen (one each at one, two four months bone healing time) three images are presented in the following figures: (a) the composite optical image of the specimen, (b) the plane strain elastic modulus map, and (c) the combined optical-mechanical map.

In cases where the indentation test location was clearly (based on both the optical and mechanical information) on the polymeric embedding resin instead of the bone, the symbol has been changed from a square to a circle and these points have been excluded from further data analysis. (These circles all correspond to modulus values of 7.5 GPa or less, associated with the polymer with a modulus of 4-5 GPa.) In some locations, no square symbol is presented on the image; in this case, the indentation test failed to run and that location and no mechanical information is available.

These images will be further discussed en masse following presentation of the three sets of images.

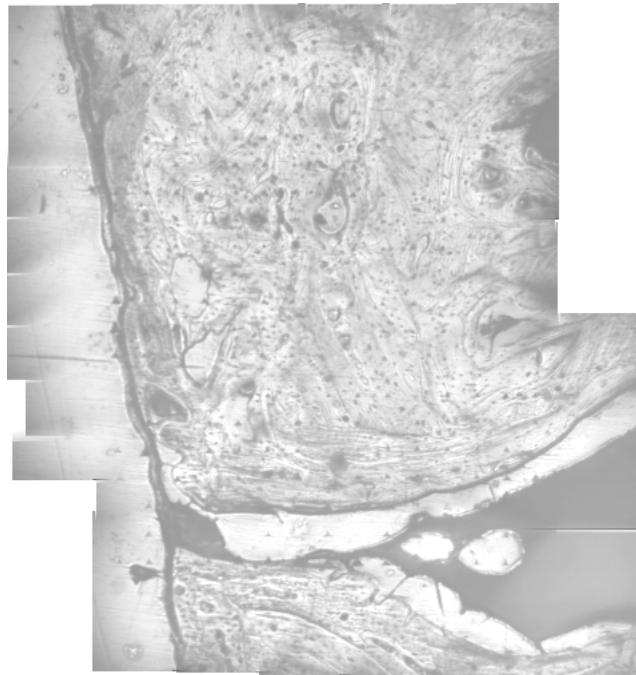


Figure 3- 27 (a): Composite optical image for bone specimen following one month healing after implantation of a dental implant. The bone-implant interface is along the left-hand side of the image.

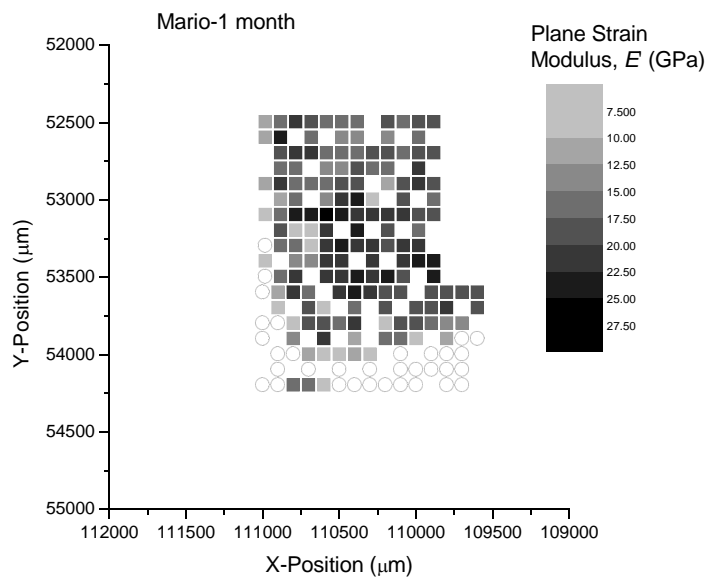


Figure 3-27(b):Plane strain elastic modulus map for 1-month sample in 3-27(a).

Mario (1 month)

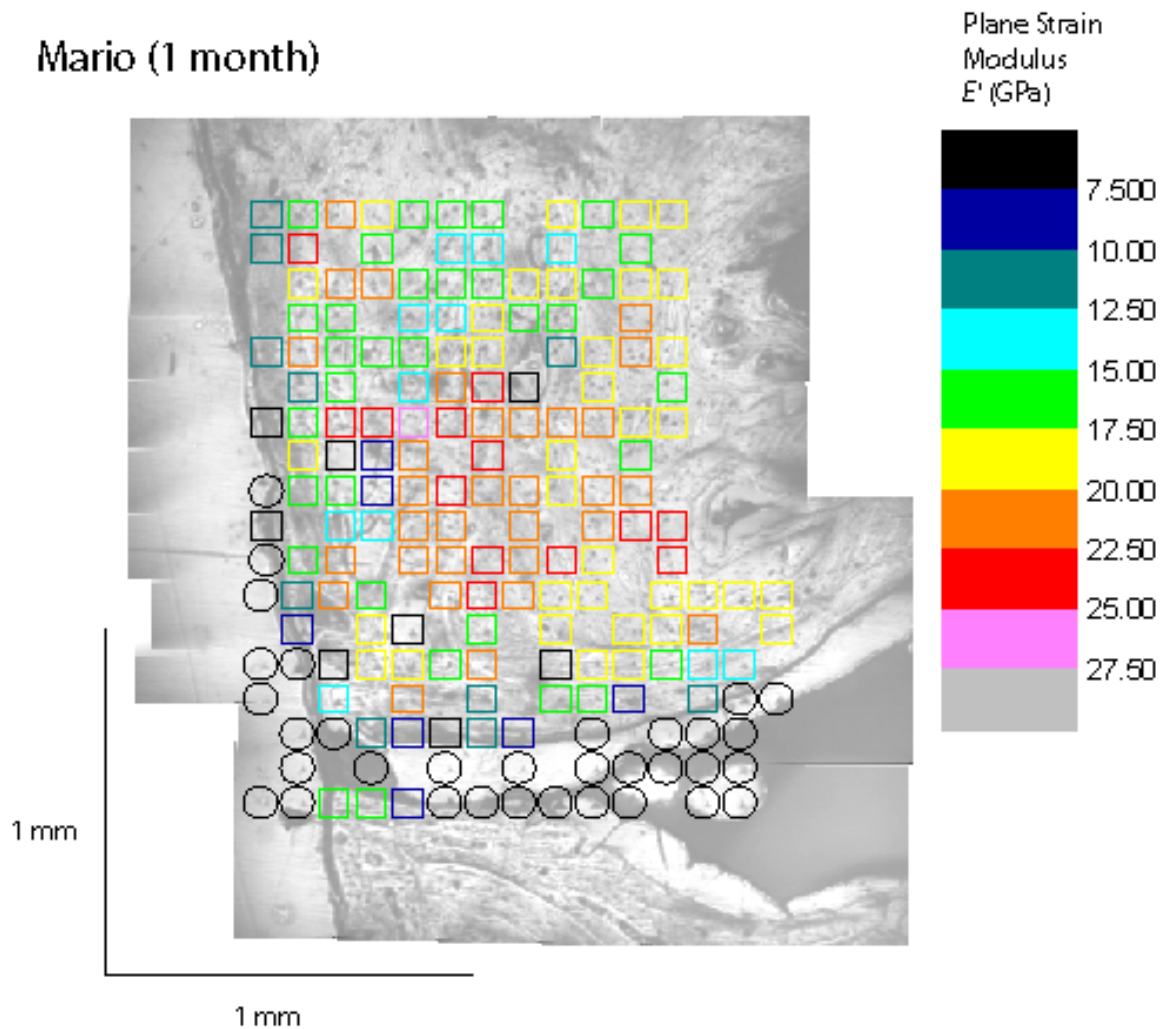


Figure 3- 27(c): Overlay image of the combined optical and mechanical information contained in parts (a) and (b)

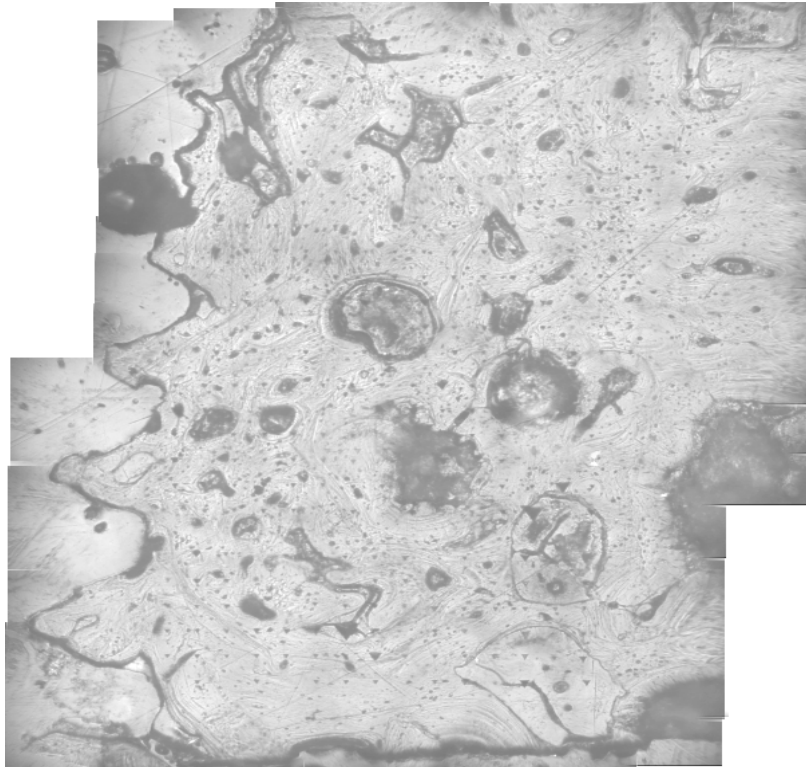


Figure 3- 28 (a): Composite optical image for bone specimen following two months healing after implantation of a dental implant. The bone-implant interface is along the left-hand side of the image.

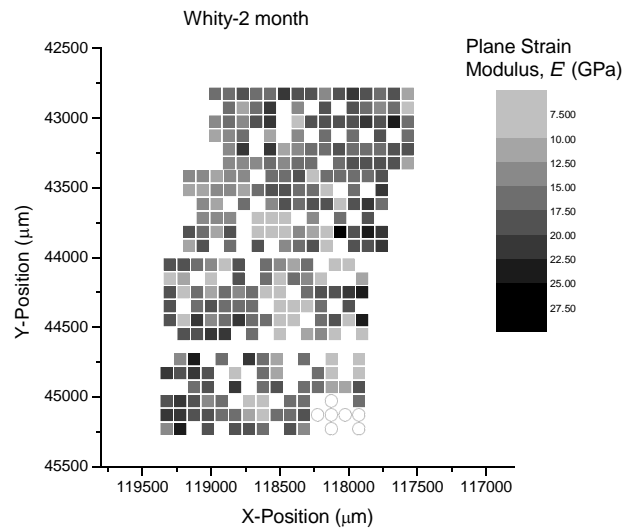


Figure 3- 28(b):Plane strain elastic modulus map for 2-month sample in 3-28(a).

Whity (2 months)

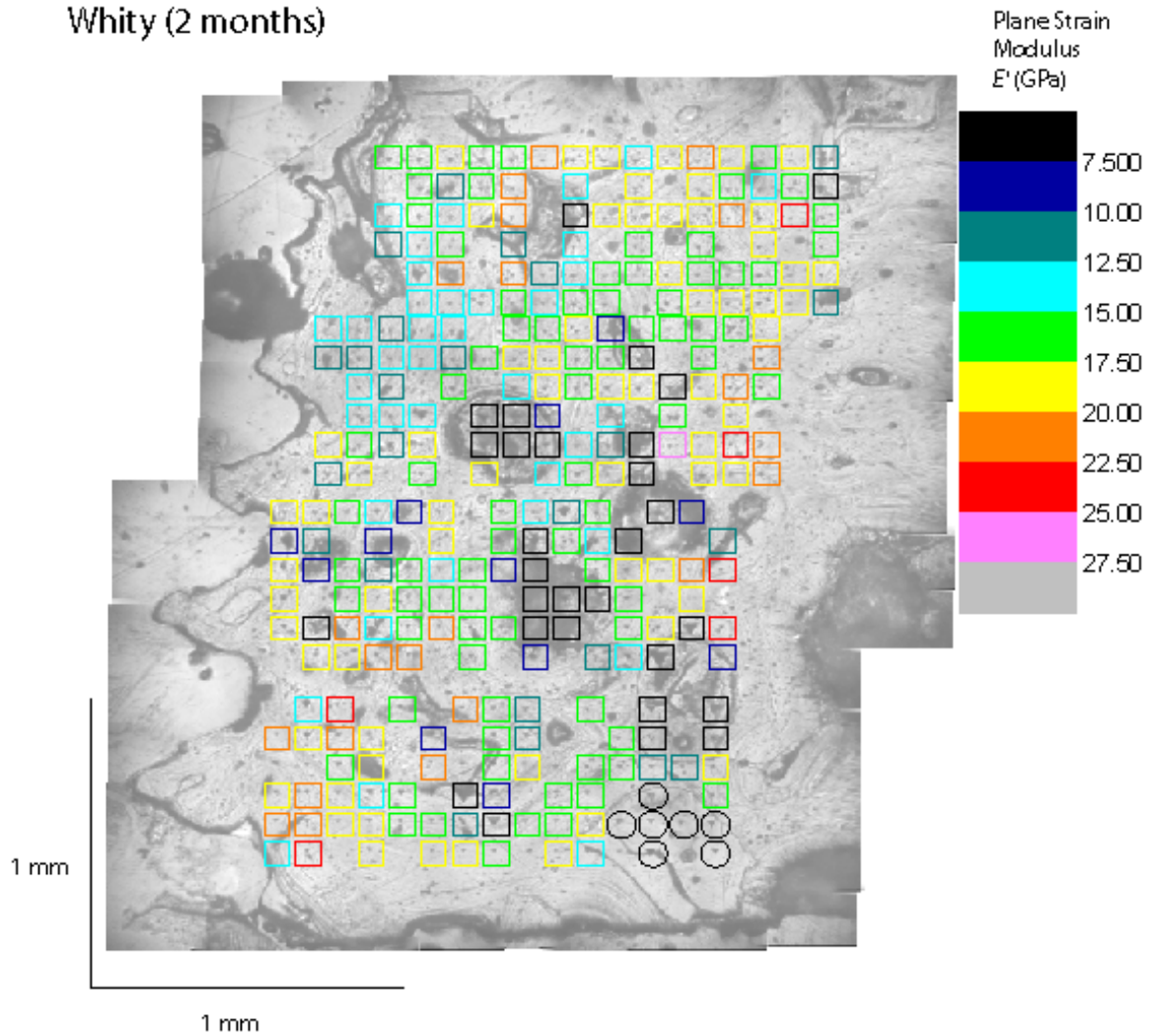


Figure 3- 28(c): Overlay image of the combined optical and mechanical information contained in parts (a) and (b)

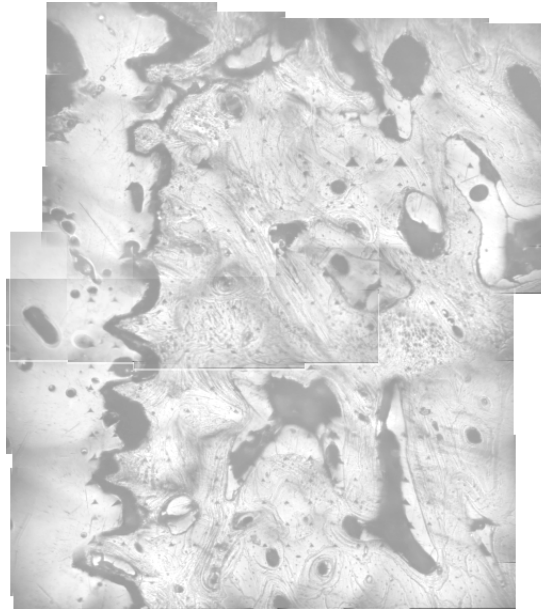


Figure 3- 29 (a): Composite optical image for bone specimen following one month healing after implantation of a dental implant. The bone-implant interface is along the left-hand side of the image.

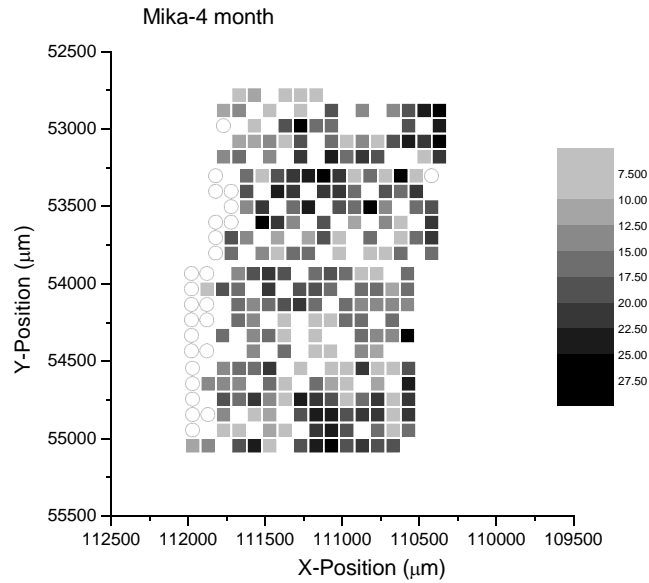


Figure 3-29(b):Plane strain elastic modulus map for 1-month sample in 3-29(a).

Mika (4 month)

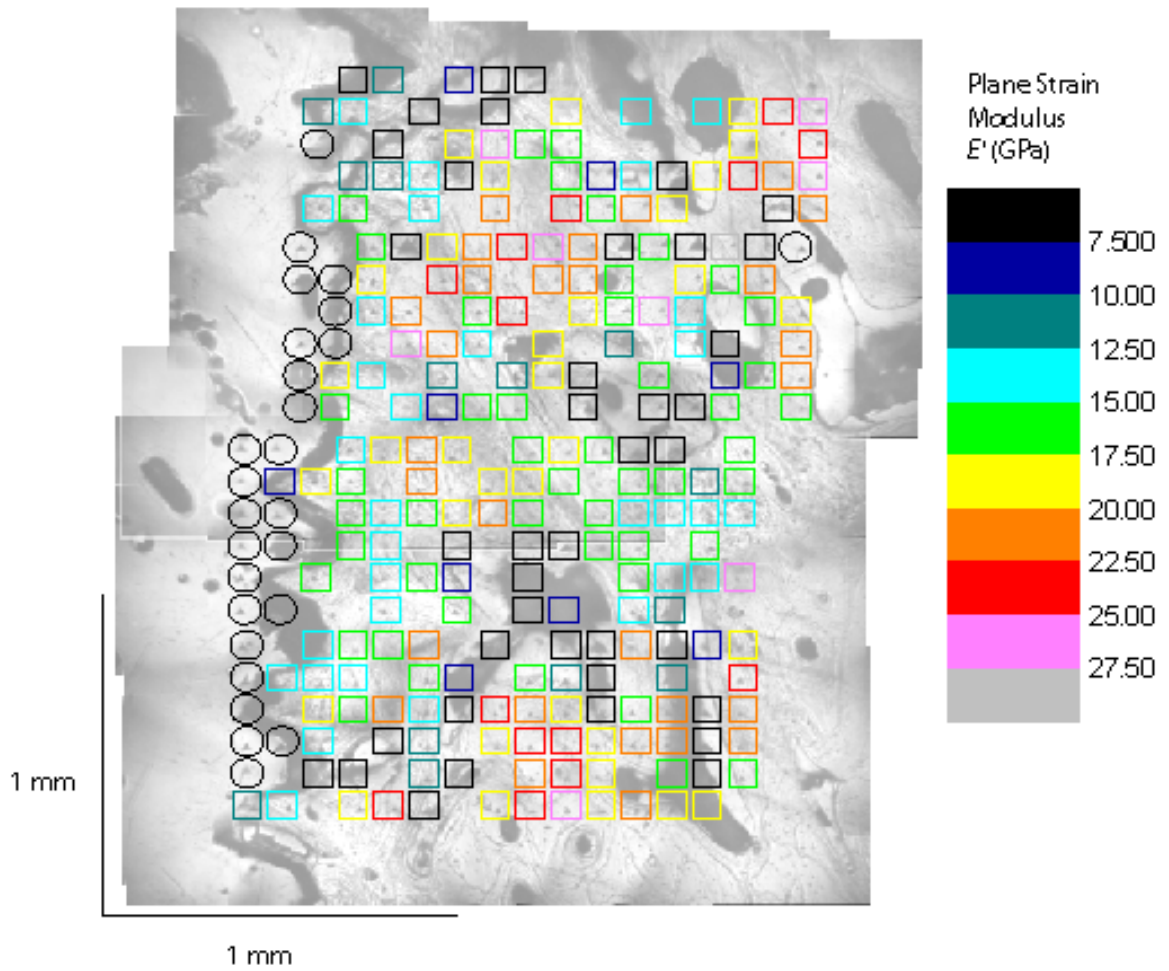


Figure 3-29(c): Overlay image of the combined optical and mechanical information contained in parts (a) and (b)

The bone specimens contained more optically-resolvable features than the DEJ sample described previously (Section 3.4.1) and the composite optical images were both easier to generate using Adobe photomerge and contained fewer interference fringes. In addition, the indentation residual impressions are clearly visible on the bone specimens, and are larger than in dentin due to the smaller values of modulus and hardness, making the registry between optical and mechanical images even simpler than in the DEJ study.

There are gaps in the information where an indentation test did not successfully run. Ironically, this problem is a known issue with the automation of the indentation instrument, and is the direct result of the variability of the bone sample. This is evident by the fact that there were few gaps in the DEJ map. There are instrument adjustments that can be made to increase the “success rate” for indentation locations, but these adjustments increase the total period of time required to generate a modulus map by increasing the amount of time required to perform each test. Each set of modulus results in the maps of Figures 3-27 to 3-29 took approximately 48 hours of block-running nanoindentation machine time to acquire. For a biological tissue at room temperature, the possibility for degradation in the material with longer testing time frames cannot be ignored, although this does not appear to be the case in the data presented here (no systematic trend for modulus with y-direction distance is apparent in the maps). Thus, there is a trade-off in this technique, in that a higher “success rate” requires a longer time to acquire the property map.

In the two-month healing bone sample (Figure 3-28), the indentation array was inadvertently started a small distance away from the bone-implant interface, and no indentation tests were run on the bone that was positioned directly between the dental implant screw threads. Future studies will aim to replicate the data shown for four-month healing (Figure 3-29) in which the array covered the implant interface region completely. This does, however, come at the expense of “wasted” indentation tests that lie on the polymer embedding resin in the interface vicinity.

There were some interesting correlations between the elastic modulus data and features in the bone. Clusters of very low-modulus results were frequently observed in a

region clearly differentiable from the surrounding bone, typically darker in the optical image. Overall, modulus data from directly adjacent tests were frequently comparable, and the largest variations were over a distance larger than the 100 μm indent spacing. However, there was no blindingly obvious trend in modulus with distance from the implant interface in any of the samples.

A histogram is presented in Figure 3-30 for the modulus information contained in the three images 3-27 to 3-29. In contrast to the histograms presented earlier (Figure 3-15) for a larger group of samples at each time-point (including these three samples), the data from the current investigation were not well-described by a normal distribution.

The results in section 3.2.2 for a different series of MTS nanoindenter tests on two different 1-month dry bone samples showed an average modulus of 17.9 GPa, in good agreement with the current average 17.2 GPa at 1-month healing. However, and also quite interestingly, the mean modulus values for the current study demonstrated an opposite trend to that seen in the previous Hysitron study on these same samples (Figure 3-15). In the previous study, the 1-month data are depressed compared to the 2- and 4-month data. In the current study, the 1-month data are, on average, elevated compared to the 2- and 4-month data. However, since the bottom line continues to be that there is large variability in the indentation modulus of bone, it is difficult to discern if this trend is real or is merely a sampling error.

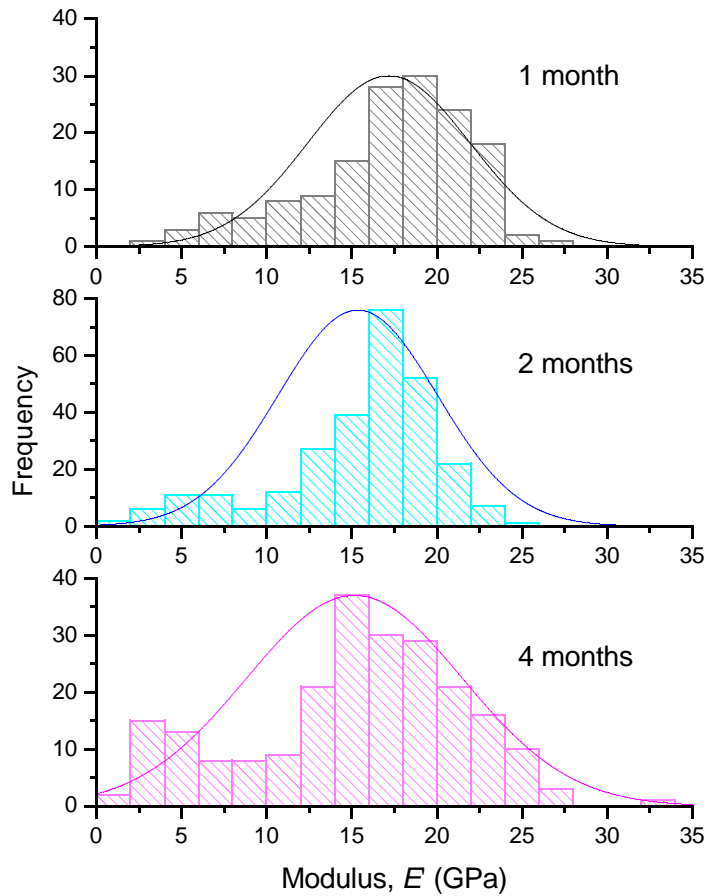


Figure 3-30: Frequency histograms for modulus (E') values after bone healing for 1, 2, and 4 months (data from Figures 3-30 to 3-32).

The mapping technique developed here, if used over large regions of many more samples from this bone study, may be what is required to better understand the overall picture. At this point, it is still unclear if these samples demonstrate trends in elastic modulus with distance from the bone-implant interface, or trends in bone modulus with increased healing time.

3.5 Discussion

The focus of this chapter has been on elastic-plastic analysis in indentation testing. The Oliver-Pharr analysis for conical-pyramidal indentation in elastic-plastic solids is extremely popular, especially since the analysis is built directly in to commercially available indentation testing instruments (including both of those described in section 2.1.6 of this work). For large scale analysis of samples, such as the property mapping performed here in section 3.4, the use of an automated instrument and the built-in elastic-plastic analysis results in extremely quick and effective materials property determination compared to traditional testing modalities. The probe-based technique, allowing for individual measurements to be made at 100 μm centers, presents interesting opportunities for gaining information about the local structure-properties relationships in inhomogeneous materials, such as mineralized biological tissues.

In order to gain quantitative information from indentation testing, the tip area calibration is extremely important. However, interestingly enough, the calibration for performing tests on compliant materials is a bit more forgiving than that required for stiffer materials, as the total displacements are large relative to any blunting in the tip (that is characterized by area function coefficients C_1, C_2, \dots). A perfect tip assumption ($C_0 = 24.5, C_1 = C_2 = \dots = 0$) is probably acceptable for large-depth indentation testing, and is certainly preferable to error associated with incorrect calibration techniques. The issues that arise in the tip calibration are somewhat machine-manufacturer dependent, but it was demonstrated in this work that with appropriate calibration (and an approximation for the difference between wet and dry samples) the indentation results from different machines are in fact comparable (section 3.2.2).

Variability in indentation responses can be assessed by examining point-to-point variations at different peak load (and corresponding peak depth) levels (section 3.3.2) as well as directly assessing location-dependent properties through a mapping technique (section 3.4). Overall, these examinations demonstrate that there is dramatic variability in the local indentation response of bone and not in dentin. Thus, a substantial difference

between dentin and bone was also found, even though their compositions are similar, indicating structure as the differentiating quality between the tissues. The dentin modulus values can be mapped using the same modulus scale as was used for the bone images (Figure 3-31), allowing for direct comparison between the bone and dentin. The optical images of the two tissue types support the difference found in property variability: the dentin is practically feature-free under optical imaging conditions while the bone contains many features. The combined optical-mechanical maps presented in this chapter allow for some level of understanding of the point-to-point variability in bone properties.

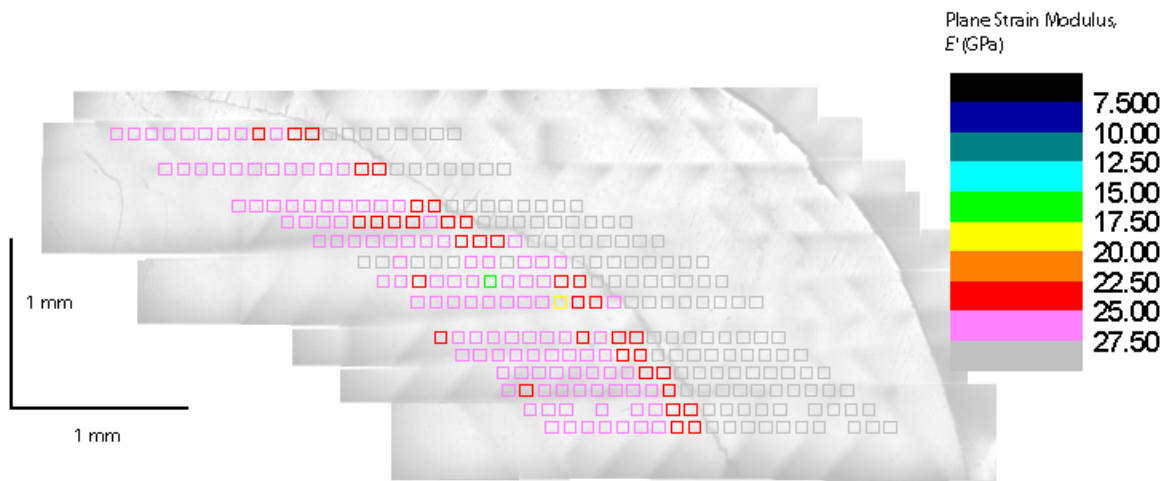


Figure 3- 31: DEJ modulus map (Figure 3-25) with the scale set to the modulus scale used for bone (Figs. 3-27 to 29 parts (c)). The dentin shows little heterogeneity on this scale. (Contrast in the base optical image has been reduced for easier visualization of the points)

Structural and compositional factors will be identified and explored as the sources of the observed property variability and will be discussed further in Chapters 5 and 6. First, however, will be an examination of the potential influence of time-dependent mechanical behavior on the indentation responses of mineralized tissues, particularly bone and dentin with their significant volume fraction of hydrated organic material.